

# Testing different explanations for the Fermi GeV-excess

Master Thesis of

Leo Bosse

At the Department of Physics  
Institut for experimental particle physics  
(ETP)

Reviewer: Prof. Dr. Wim de Boer  
Second reviewer: Prof. Dr. Ulrich Husemann

Duration: 1. March 2017 – 10. April 2018



---

I declare that I have developed and written the enclosed thesis completely by myself, and have not used sources or means without declaration in the text.

**Karlsruhe, 9th May 2018**

.....  
**(Leo Bosse)**



# Contents

<b>Introduction</b>	<b>1</b>
<b>1. Theory</b>	<b>3</b>
1.1. Our Milky Way . . . . .	3
1.1.1. General properties . . . . .	3
1.1.2. Dark Matter . . . . .	4
1.2. Spectrum description and vocabulary . . . . .	6
1.3. Physics of Cosmic Rays . . . . .	7
1.3.1. Creation of CR . . . . .	7
1.3.2. Energy losses . . . . .	7
1.3.3. Propagation of CRs . . . . .	8
1.3.4. Effect of molecular clouds . . . . .	9
1.3.5. CRs as observed from Earth . . . . .	9
1.4. Physics of gamma-ray . . . . .	10
1.4.1. Gamma-ray creation . . . . .	10
1.4.2. Gamma-ray observations . . . . .	11
1.5. Unresolved problems of gamma-ray observations . . . . .	13
<b>2. Method</b>	<b>15</b>
2.1. Data origin . . . . .	15
2.2. Model components . . . . .	18
2.2.1. From CRs to gamma-rays . . . . .	18
2.2.2. Basic components . . . . .	18
2.2.3. Additional components . . . . .	19
2.3. Fitting method . . . . .	22
<b>3. First results: Study of the excess</b>	<b>25</b>
3.1. Recreating previous results . . . . .	25
3.1.1. EGRET Data . . . . .	28
3.2. Introducing SCR . . . . .	29
3.3. Introducing an excess component . . . . .	31
3.3.1. Introducing MCR . . . . .	31
3.3.2. Introducing DM . . . . .	32
3.3.3. Introducing MSP . . . . .	34
3.4. Discussion on previous results . . . . .	35
3.4.1. Detailed comparison of the excess spectral shape . . . . .	36
3.5. Correlation between the excess and molecular clouds . . . . .	37

---

<b>4. To go further: How to improve the model</b>	<b>39</b>
4.1. Discussion on the spatial distributions of the other components. . . . .	39
4.1.1. PCR flux distribution . . . . .	39
4.1.2. IC flux distribution . . . . .	41
4.1.3. BR flux distribution . . . . .	42
4.1.4. SCR flux distribution . . . . .	43
4.2. Correlation between SCR, MCR and point sources . . . . .	44
4.3. Adding an break in electron CR spectrum . . . . .	45
4.4. Mixing MCR and DM . . . . .	47
4.4.1. DM and MCR in the same fit . . . . .	47
4.4.2. Adding DM afterwards . . . . .	48
<b>5. Conclusion</b>	<b>49</b>
<b>Acknowledgments</b>	<b>51</b>
<b>Bibliography</b>	<b>53</b>
<b>Appendix</b>	<b>59</b>
A. Method . . . . .	59
B. First results: Study of the excess . . . . .	65
C. To go further: How to improve the model . . . . .	69

# Introduction

Cosmic Ray (CR) physics started in the early 20th century with the study of the atmospheric ionization. First, highly energetic particles were believed to be linked to the Earth's natural radioactivity. The first to point out the extraterrestrial origin of the atmosphere ionization was Victor Hess in 1912, when he sent an electrometer in a balloon to high altitudes. The fact that the ionization increased with altitude was a surprise and its discovery gave him a Nobel Price. Multiple studies have then confirmed and refined the results. CR origin and composition was unknown for a decade, until the 30's where discoveries multiplied. First thought to be gamma-rays, anisotropies in their arrival direction indicated a higher proportion of positively charged particles, protons, as later balloons experiments identified. It was also during that time that particle showers were detected for the first time and showed the very high energy of CR. No experiment on Earth was able to recreate such energies to this day, so their study is complicated and often based on indirect observations. This makes these particles the only means of studying highly energetic physical phenomena, either at small scales for particle physics or very large for astrophysics, and both are strongly linked together.

Even though their collision processes are relatively well known, their origin still presents many mysteries. Identifying CR sources precisely is a hard task and is still subject to many studies today. One of the first ideas was supernovae, and many other candidates have joined the list, such as pulsars, quasars and gamma-ray bursts. The understanding of these processes could teach a lot about every one of these powerful objects, and contribute to the understanding of the universe.

There exists a few processes for CR particles to interact in space, and these are known and can be studied on Earth. These processes are sources of indirect particle creation, particularly gamma-rays that can be used for indirect detection methods. These high energy photons are useful because they travel in a straight path, but observations and theories do not match perfectly yet. Especially near the galactic center, an excess of gamma-rays is observed that cannot be explained. The high density of matter, radiation and processes happening in that region leave many possible interpretations. And, as expected, several hypotheses on the origin of the excess already exist, some of them going beyond the standard model of particle physics.

The goal of this thesis will be to compare the three main hypotheses to explain this excess, namely dark matter annihilation, millisecond pulsars and molecular clouds cut-offs. The study will be based on data-driven methods and try to decide which theory seems most likely. The entire gamma-sky will be fitted to our model in a large energy range, enabling spectral and spatial studies. Some of the early results can be found in the literature [1]. If one of the three hypotheses stand out from the others, later improvements can be made to refine the study even further.

The following chapters will first present the detailed theory behind cosmic-ray physics, relevant for the rest of the thesis. Then the scientific method used to obtain the results will be detailed. This will lead to the first results in themselves and discussions on their meaning and relevance. Finally, an examination of possible changes to the model that could improve the results will introduce the final conclusion.

# 1. Theory

## 1.1. Our Milky Way

### 1.1.1. General properties

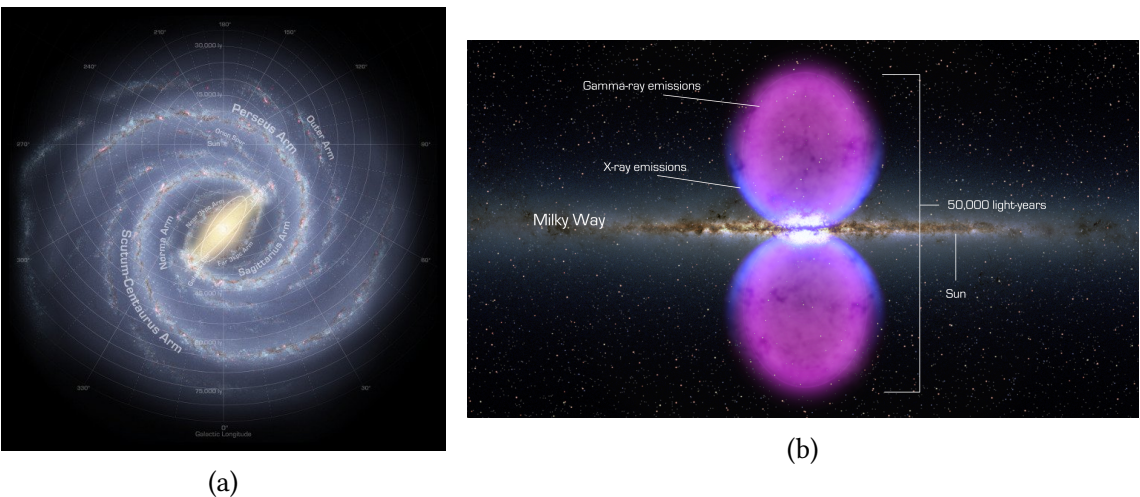


Figure 1.1.: The Milky Way, as seen from two different angles. (a) As seen from "above", the barred spiral arm structure is visible. As seen from Earth, the central bulge extend from circa -20 to 30 degrees. The image is taken from [2] (b) Looking from the side, the disk is very thin, especially stars and dust, but gas is thicker, as well as the bulge. Two large bubble-like structures extends north and south from the galactic center, composed of high energetic particles. The picture is taken from [3]

For a long time, people thought the universe was constituted of only one galaxy, the Milky Way, the one in which the Sun and the Earth orbit. The discoveries of other galaxies in the universe came only in the 20's thanks to Edwin Hubble [4]. There are still unanswered questions about these objects, but the Milky way is well known and will play a major role in the focus of this thesis. Its shape, density and composition are three main factors playing a role in cosmic ray physics and cannot be avoided.

The Milky Way is a barred spiral arm galaxy, meaning it has two main spiral arms, connected in their center by a straight galactic bar. Those arms and bar are defined by a higher matter density, due to the orbits of stars around the center. Its diameter exceeds 40 kpc for a mass of around  $10^{12} M_{\odot}$  and a thickness of under 1 kpc [5]. The Sun and the Earth are orbiting 8 kpc from its center, doing a complete rotation in 240 Myr. All the different objects of the galaxy can be found in this thin disk of matter, mainly in the spiral arms. It includes the stars, planets and other massive objects, but also dust and gas clouds. As seen from Earth, the disk looks like a narrow band, a few degrees wide, but with a very high concentration of stars, gas and dust. In 2010, two large scale structures were detected to the north and the south of the galactic center (GC) [6] [7]. With a diameter of 7 kpc, these two "bubbles" extend up to 40 degrees in latitude and 20 in longitude. They are a source of high energy gamma-rays and were detected by the Fermi Large Area Telescope (LAT) (Fig. 1.1b).

The disk of the Milky Way is composed of matter in different forms, like stars, gas or dust. Stars are one of the main source of the interstellar radiation field (ISRF). They can be modeled as black body radiating at different energies depending on their temperature. They are the main source of ultra-violet (UV) photons that play a major role in gas evolution and composition. Stars are forming inside gas and dust clouds collapsing on themselves under their own gravitational pressure. The gas is mainly composed of hydrogen, but heavier elements and even molecules can be found at the center of large dust and gas clouds where UV light cannot penetrate. One of these is the CO molecule, often used as a tracer of molecular clouds [8] [9]. Molecular clouds (MC) will be used to designate large regions of gas and dust which can possibly contain stars inside. Dust is also present in the galactic disk, for a total mass a hundred times smaller than the total mass of the gas [10]. It can be warmed up by starlight, and then radiates infrared (IR) light. This IR source also contributes to the ISRF.

An electromagnetic field is present all across the milky way, generated by rotating stars, molecular clouds, or plasmas. It has been observed and measured, but it is complex and has no distinct direction at small scales (interstellar scale). Its complexity makes it impossible to measure precisely in every point of the galaxy, and impossible to model. The most common representation at small scales is still given by a random field direction.

### 1.1.2. Dark Matter

The shape of spiral galaxies is well known today, with thousands of observed examples throughout the universe. This knowledge is used to mathematically model them, and in particular the rotation speed as a function of the distance respective to the center. It was a big surprise when the observed angular speed did not match the theory [12], as shown in figure 1.2. The expected curve (in blue) shows a decreasing rotation speed above a 2 kpc radius, while the observed curve (in red) flattens out and falls off steeply. One of the explanation for this difference is the introduction of dark matter (DM), which brings a lot of invisible mass into the galaxy. It still is not observed and a few theories exist on its exact nature [13]. Even if its exact nature is not known, its mass distribution can be deduced from the observed rotation curve of the galaxy. The predicted distribution is a spherical halo extending beyond the 40 kpc of the galactic disk. Its density peaks in the GC, and decreases with the radius following a given density profile. The exact profile is not known. A currently investigate parametrization of it is the Navarro-Frenk-White (NFW) profile defined as follows :

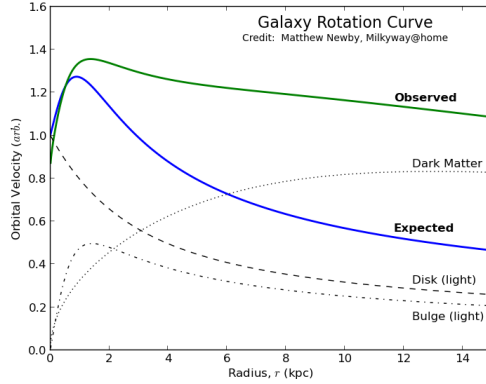


Figure 1.2.: Orbital velocity of the Milky Way as a function of the distance from the GC. A clear discrepancy between the expected (in blue) and the observed (in green) velocity can be seen above a 2 kpc radius. The expected velocity drop too low above 2 kpc, when the observations show a flat curve. The blue curve is the sum of the predictions from the disk and the bulge, both composed of standard matter. But adding the predictions for dark matter to the blue curve, the theory would match much better the observations. [11] [12]

$$\rho(r) \propto \frac{1}{(r/r_S)(1+r/r_S)^2} \quad (1.1)$$

where  $r_S$  is the scale radius, determining the size of the halo. [14]

One of the most popular explanations of DM is the Weakly Interacting Massive Particles (WIMP) theory [15]. These particles are supposed to be non-standard particles with a large mass, neutral, and only sensitive to the weak force, making them difficult to observe. No particles of the standard model are valid candidates, or could provide the amount of mass needed to speed up a galaxy. It is predicted that two WIMP colliding could produce gamma-rays, providing enough mass and energy. This gamma ray radiation is proportional to the WIMP density and cross-section, thus following the DM halo distribution.

## 1.2. Spectrum description and vocabulary

To speak about CRs, one often speaks about their spectral shape, or energy spectrum. These terms refer to the energy flux  $\Phi$  in  $\text{GeV}^{-1} \text{ s}^{-1} \text{ cm}^{-2} \text{ sr}^{-1}$  as a function of their energy. It describes how many particles of a given energy would be observed in a second by a one centimeter square instrument with an opening angle of one steradian. This can often be modeled by a power law of the form  $\Phi \propto E^{-\alpha}$  where  $\alpha$  is called the spectral index. Lower values of  $\alpha$  results in a "hard" spectrum, because of the important proportion of high energetic particles. This designation comes from the fact that the path of highly energetic particles are "hard" to bend. On the contrary, a "soft" spectrum has a bigger spectral index and describe a lower density of high energy particles compared to low energies. The terms "soft" and "hard" can be applied to any kind of energy spectrum, even if it is not a power law, it will only describe the relative proportion of high and low energy particles.

In the following chapters though, the preferred representation of the energy distribution is via the energy flux, or spectral energy distribution in  $\text{GeV s}^{-1} \text{ cm}^{-2} \text{ sr}^{-1}$ , simply obtained by multiplying the particle flux by its energy square ( $E^2 \times \Phi(E)$ ). In other terms, how much energy does the instrument receive every second for particles of a given energy. This is only done to facilitate the reading of the graphs and does not affect the underlying physics.

A useful parameter to describe a CR particle is its rigidity, defined as its total energy divided by its charge and given in Volts. It describes the way a particle's path can be bent by an electromagnetic field. On the one hand, the momentum makes a particle go in a straight line. On the other hand, the electromagnetic force applied on it will deviate its trajectory. The higher the rigidity, the less impact an electromagnetic field will have on the motion of the particle. On the contrary, if the rigidity is low, the particle will follow the field lines.

## 1.3. Physics of Cosmic Rays

### 1.3.1. Creation of CR

Several sources of Cosmic Rays exist in the universe. CR can be highly energetic and thus can only be produced by large astrophysical bodies. Particularly powerful events are supernovae, ejecting relativistic particles during the burst. The dying star ejects a lot of its mass, forming a supernova remnant (SNR) surrounding either a white dwarf, a neutron star or a black hole depending on the initial mass of the star. These SNR could also play a role after the explosion via the Fermi process; it is to say that an already energetic particle would bounce in the shock wave created by the explosion, and gain energy via magneto-hydrodynamic processes before escaping when a threshold energy is attained. [16] Another important source of CR are pulsars. These rapidly rotating neutron stars and their intense electromagnetic field accelerate high energy particles such as electrons and positrons. This can last as long as the pulsar rotates fast enough, from 10 to 100 Myrs, before slowing down. A third source are the active galactic nuclei (AGN), also known as quasars. These objects consist of a super-massive black hole at the center of a galaxy. First discovered thanks to their radio emission, they are also able to eject CR, via Fermi or centrifugal acceleration.

All these sources can be traced via  $^{26}\text{Al}$  observations [17]. The radioactive  $^{26}\text{Al}$  isotope is synthesized by proton capture of  $^{25}\text{Mg}$  in heavy, magnesium rich sources and can be traced by the 1.8 MeV gamma-line emitted in its decay. This line has been studied by the Integral/Spi satellite [18] and is publicly available as sky map. [19]

### 1.3.2. Energy losses

Traveling through the galaxy particles interact with different objects and can gain or lose energy during the event. Every time a particle collides with another less energetic particle, or is deflected by a magnetic field, it loses energy. Depending on its energy and its surroundings, a particle will not always lose energy at the same rate. A useful way to rate the impact of these interactions is through the energy losses time, defined as the time it would take for a particle of a given energy to lose all of it (see Fig. 1.3). This gives an insight on the average propagation length for CR particles.

If the particle has a high enough energy, it will mainly encounter lower energy particles and will lose energy faster than low energy particles. If a low energetic particle is in an environment where all the other particles have about the same energy, every collision will only change its energy a little, and it will basically stay the same. This process is very important for electrons and positrons, which have a lower mass than nuclei. A second phenomenon occurs for high rigidity particles, mainly protons and heavier nuclei. The highest energetic particles will escape the Milky Way quickly because the magnetic field is not strong enough and collisions are too sparse to retain them inside. This way, the lower the energy of a particle, the longer it will stay inside the galaxy [20]. These two processes are important to explain changes in the CR spectral index. The high energy particles emitted directly at the source will lose energy or escape faster than the less energetic ones, thus enhancing the lower part of a spectrum. This way, a propagated population of CR has a softer spectrum than it had when emitted by its source.

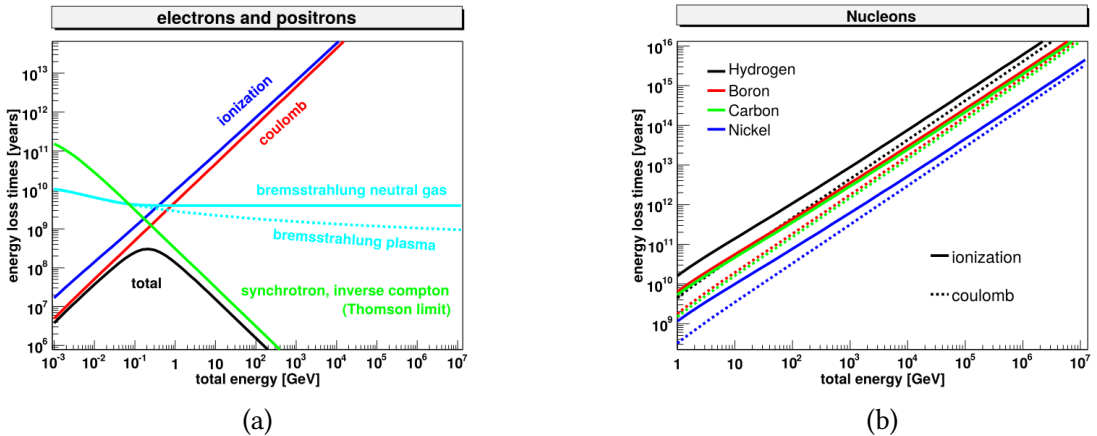


Figure 1.3.: Illustration of energy losses times of different particles as a function of their total energy calculated for a hydrogen density of  $0.01 \text{ cm}^{-3}$  (from [21]). (a) Electron and positrons energy loss times. They are dominated by ionization and Coulomb interactions below 0.2 GeV, and dominated by synchrotron and inverse Compton above. 0.2 GeV is the energy for which the particle will lose its energy at the lowest rate. (b) Protons and heavier nuclei energy loss times. Only ionization and coulomb losses are relevant. High energy CR nuclei lose their energy slower than low energy CRs, but they escape the Milky Way quicker [20].

### 1.3.3. Propagation of CRs

Once they are emitted, the CR propagate through the galaxy under the influence of different interactions. The first thing to consider is the complex magnetic field running through the galaxy. It is not particularly strong, on the order of micro-gauss [22] [23], compared to the heliosphere or what can be created on Earth [24], but its very large scale suffice to bend the CR's path in all direction until the point where it is impossible to backtrack their origin. This magnetic field takes its origin in large scale structures of the galaxy, but a lot of sources create small scale turbulence. Every star creates its own magnetic field via the dynamo effect [25], changing in intensity and direction over the years, as what has been observed with the Sun [26]. Molecular clouds and ionized gas regions create their own field [27] on relatively small scales. Self-generated turbulence can also arise when plasma, or charged particles in general and magnetic field interact with each other. All these small-scale structures play a role in low energetic CR diffusion make it impossible to backtrack a particle.

Another possible interaction is the collisions with other particles. It depends on the density distribution of those colliders along the path of CRs. For example, a higher number of collisions in the disk is expected, where the density of molecular clouds is the highest.

All these influences can be modeled by a diffusion equation (Eq. 1.2) [28], mainly defined by its diffusion coefficient  $D$ , which describes the average distance away from the origin traveled by the particles before scattering occurs. The higher the coefficient, the faster a particle will diffuse in the galaxy. On the contrary, if  $D$  is small, the particle's path will be bent in every direction so often that it stays close to its source for a longer time.

$$\frac{\partial}{\partial t} n_p(E, \mathbf{r}, t) = -\nabla \cdot [D(R, \mathbf{r}, t) \nabla n_p] - \frac{\partial}{\partial E} [b(E, r, t) n_p] = Q(R, \mathbf{r}, t) \delta^3(\mathbf{r} - \mathbf{r}_g) \quad (1.2)$$

where  $n_p(E, \mathbf{r}, t)$  is the space density of particles p with energy E at time t and point  $\mathbf{r}$ ,  $D(E, \mathbf{r}, t)$  is the diffusion coefficient,  $b(E, \mathbf{r}, t) = -dE/dt$  is the continuous energy losses, and  $Q(E, \mathbf{r}, t)$  is the source function, or the flux of particle emitted by a point source located in  $\mathbf{r}_g$ .

While the diffusion coefficient for the galactic magnetic field can be taken as constant throughout the Milky Way [23], the diffusion coefficient due to collision is proportional to the particles density. A smaller coefficient in molecular clouds is expected, where the density of particles can reach  $10^{15} \text{ cm}^{-3}$  in the core. [29]

This coefficient will also define the CR densities in various locations of the galaxy. Indeed, the more a particle's path is twisted and convoluted, the longer it will take to move away from its origin. This way, a higher density of CR can be found in low diffusion coefficient areas like molecular clouds. In comparison, the region outside the galactic disk has a low density of CR due to a weak electromagnetic field and small gas and dust density. However, the bubble region is outside the disk and has a higher concentration of high energy CR than other regions outside the disk. This is due to a direct outward emission of CRs from the GC region. With a high diffusion coefficient, these CRs are ejected light years away (see Fig. 1.1b), forming two symmetric regions extending north and south up to 40 degrees in latitude in galactic coordinates.[7]

The consequences of such diffusion processes is an isotropic CR sky on Earth. In whatever direction the instruments look at, they measure the same CR flux. This complicate CR study, since no information about their origin or their journey can be learned from direct observation, and it is why gamma-rays are useful in indirect detection methods.

### 1.3.4. Effect of molecular clouds

Molecular clouds could play a major role in the spectral distribution of CR in the disk via their magnetic field. The magnetic field around those objects can deflect charged particles. If the CR particle has a high rigidity, the effect will be negligible, but for lower rigidity, the particle's path can be bent enough so that the particle never enters the MC, as observed on Earth [30].

Another theory is investigated [31]. The electromagnetic field density in their core is greater than on the outside due to a higher density of particles. A particle entering the MC along a field line could be reflected by this increasing field density, much like it is observed on Earth with the Earth magnetic field.

In both cases, the result is the same. Low energy CR are deflected before entering the MC, thus depleting the lower energy CR spectrum in MCs.

### 1.3.5. CRs as observed from Earth

The CR spectrum obtained from observations on Earth is shown in Figure 1.4. It is the same in every direction as far as the measurement uncertainties can tell [33]. The isotropic arrival direction of CRs is measured with great care and any anisotropy, if existing, is below the instrument precision. The CR spectrum is composed of three main features that form a "leg". The "knee" around  $10^7 \text{ GeV}$  marks the separation between two different power laws in  $E^{-\alpha}$ . A slightly harder one below that is thought to be composed of galactic CRs, and a softer one above that is supposed to be of extra-galactic origin. The spectral index changes from 2.7 below to 3 above, due to different production

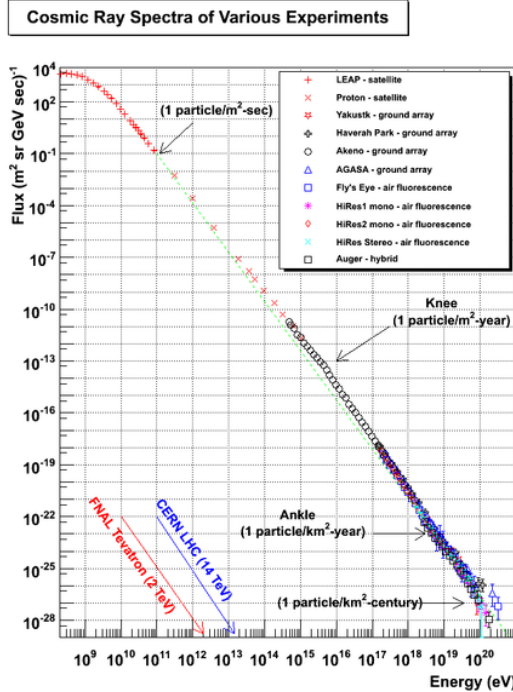


Figure 1.4.: Cosmic ray spectrum as seen by several experiments. This characteristic shape can remind a leg, with a "knee" around  $5 \times 10^{15}$  eV and two different spectral indexes on both sides. Below  $10^{10}$  eV, the spectrum flattens due to the solar and earth magnetic field which deflect low energy particles. On the other side of the spectrum, above  $10^{18}$  eV, the spectrum hardens imperceptibly, and the statistics are very low, but it is the highest energetic particles ever observed. In comparison, the red and blue arrows show two of the best human attempts to recreate very high energetic particles and give an idea how powerful CR can be. The picture was taken from [32]

mechanisms. [34] As indicated on Figure 1.4, the corresponding flux of particles is lower and statistical fluctuations are not negligible at high energies. Especially at the "ankle", above  $10^9$  GeV, where only very few particles are detected.

## 1.4. Physics of gamma-ray

### 1.4.1. Gamma-ray creation

Since the cosmic rays observed on Earth are hard to backtrack, some indirect detection methods are required to find their origin. CRs interact in a lot of ways with their environment, as described in the previous section. These interactions can leave detectable traces. The most common is the production of gamma-rays, i.e. photons in the GeV energy range. Once created, these gamma rays cannot be deflected, which make them easier to backtrack. Linking gamma-ray and CRs requires to know the main production processes which follow.

#### Pion decay (PCR)

Hadronic CRs particles interact with the interstellar medium and can lead to  $\pi^0$  production. Any CR nuclei can result in pion production, but since protons are the most

abundant particles, they will dominate the production. These newly created pion can rapidly decay into a pair of gamma-rays (99% of the time) or  $e^+e^-$  pairs, the latter being negligible.

### Bremsstrahlung (BR)

A charged CR passing near another charged particle of the ISM or in a magnetic field will be deflected by the electromagnetic interaction. In the process, the CR will lose energy via the emission of photons. The emitted energy depends on the energy of the electron and the intensity of the electromagnetic field. The more the electron is deflected, the higher the energy of the emitted photons. Even though proton CR are charged, the main sources of bremsstrahlung gamma-rays are electrons and positrons. This is due to the much lower mass of the electrons, making them easier to deflect.

### Inverse Compton scattering (IC)

When a high energy electron collides with a low energy photon, the electron transfers some of its kinetic energy to the photon, giving it enough energy to enter the GeV energy range.

The amount of gamma rays coming from Inverse Compton scattering is directly linked to the electron distribution and the ISRF of the galaxy. The latter is composed of three major components, the starlight, the dust emission and the cosmological microwave background (CMB). The first component is directly linked to the star distribution, and will be dominant in the disk, where most stars are located. The starlight follows a black body spectrum, peaking in the UV range. The dust emission comes from the infra-red emission of warm dust. It also is mainly present in the disk, following the matter distribution in the galaxy. Finally, the CMB is peaking in the microwave range but is uniformly present everywhere in the universe, and therefore in the galaxy. It is dominant where  $\pi^0$  and BR are negligible, namely outside the galactic disk.

### Other sources

The three previously described processes are general processes that can happen everywhere at any energy. Even though the processes are always the same, two classes of sources can be defined: the diffuse and the point sources. The first correspond to all the CR propagating through the ISM and interacting with its components. It will be the object of study of the following chapters. The second are the gamma-rays produced directly at the CR origin (in SNR, AGN or pulsars as described in section 1.3.1). Every one of these sources should be studied separately and are not fully understood. Since these sources cannot be resolved by the instruments, they will be referred to as point sources in the following chapters. The spectral shape of these point sources is generally known and categorized as a function of the source type. This makes their recognition possible, and diffuse and point sources emissions can be separated.

#### 1.4.2. Gamma-ray observations

On Earth, gamma-rays are absorbed by the atmosphere [35]. To measure them directly, the instrument has to be launched into orbit above the atmosphere, where gamma-rays are not yet absorbed. The Fermi Large Area Telescope (LAT) for example, maps the

gamma-ray sky between 20 MeV and 300 GeV [36], detecting all the point source emissions as well as the diffuse background emission. This telescope started operations in 2008 and is still observing. It can be thought as a sequel of the EGRET instrument [37] from the Compton Gamma Ray Observatory (CGRO). This instrument was also in orbit from 1991 to 2000 and could observe photons between 30 MeV and 30 GeV. They both helped discovering gamma-ray sources and the gamma-ray sky in general.

In theory, the knowledge of the processes that generate gamma-rays from cosmic-rays and the precise composition of the Milky Way should allow to explain the observations. Propagation models and simulations are able to output the expected energy spectrum of gamma-rays reaching Earth from an initial distribution of cosmic-rays (not taking the point sources into account). When comparing the model and the observations differences arise, as will be discussed in the following section.

## 1.5. Unresolved problems of gamma-ray observations

Several studies have already tried to see how the predictions of the gamma rays emission and the observations compare [38], [39], [40]. The three discussed processes were modeled to try to recreate the spectrum observed here on Earth. The accepted model is composed of a single spectrum of propagated proton CR, and a single electron spectrum. Then, gamma-rays are deduced and modeled from there. The results show discrepancies. Even though the observations of the galactic poles or any high latitude regions can be well explained by a propagated CR, bremsstrahlung and inverse compton scattering component, the models fail to reproduce the surroundings of the galactic disk, and in particular the GC or the bubbles. Two discrepancies can be identified. A high energy deficit in the models, where the observed high energy tail ( $> 50$  GeV) cannot be reproduced [40], and a spherical excess centered in the GC around 2 GeV.

The first one shows a lack of high energy CRs in the models. A mean of injecting more relativistic particles has to be found in order to fill this gap. One explanation is that we do not observe only diffuse emission in the disk. The point source emission could not be entirely subtracted due to the high density of sources. The CRs that did not yet propagate have a harder spectrum, thus providing a higher ratio of high energy gamma-rays. This would also happen in the bubbles, were CR are injected without propagating in the disk first.

Two main ideas have emerged to explain the spherical excess. First is the presence of dark matter in the galaxy in the form of weakly interacting massive particles (WIMP). The spatial distribution of these particles would follow a NFW profile centred at the GC. They are also expected to produce gamma rays when annihilating with each other via hadron production. In theory, if the mass of a WIMP particle is around 50 GeV, the expected gamma spectrum would peak around 2 GeV, where the excess is observed. [38], [39] The study of the excess could put strong limits on the mass and annihilation cross section of such WIMPs and confirm, or reject the theory. The second theory does not involve new physics, but unobserved millisecond pulsars. They would also be spherically distributed around the GC and their gamma spectrum peaks around 2 GeV. A few thousand of them would be needed to recreate the intensity of the excess [39]. The main default of this explanation resides in the fact that we have observed only a few hundreds pulsars so far when we expect ten times more to explain the excess.



## 2. Method

### 2.1. Data origin

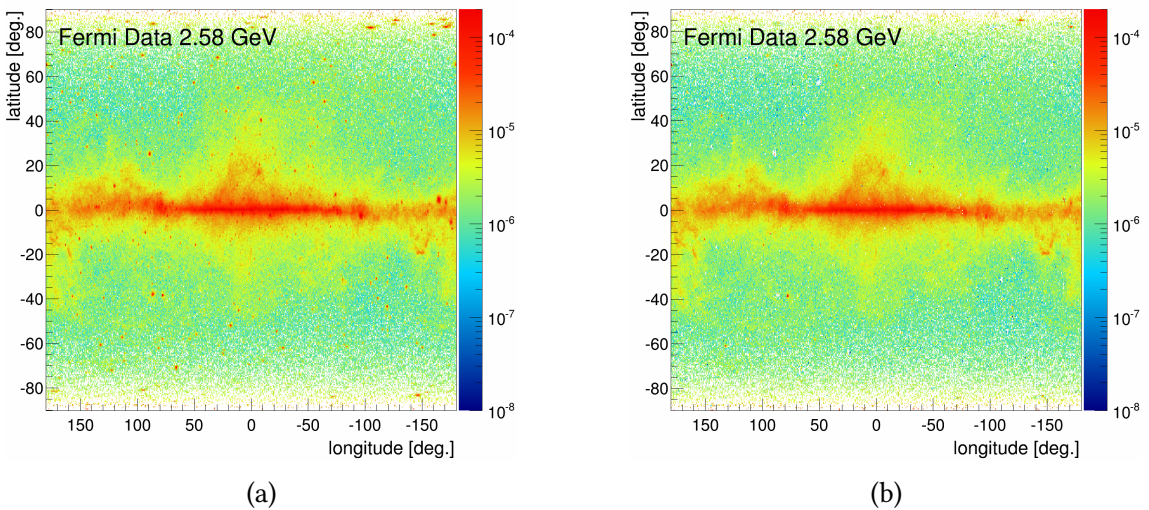


Figure 2.1.: Map of the gamma ray sky as seen by the Fermi telescope around 2 GeV. Measured gamma ray flux before (left) and after (right) point source subtraction in  $\text{GeV}/\text{s}/\text{m}^2/\text{sr}$ . Most of the spots formed by point sources have disappeared, leaving only the diffuse background emission from CR. The subtraction does not remove all point sources, and can create artificial "holes" in the map (for example at coordinates (90, 25) or (50, 60)). These can be disregarded as relevant data, or can also disappear when using a larger binning.

All the following work is based on the measurement of gamma rays coming from intra- and extra-galactic sources. The quality and accuracy of the data is one of the most important points that will determine the general quality of the results. Thus it is capital to be certain that the gathering and treatment were done properly.

The Fermi Large Area Telescope (LAT) observes the gamma-ray sky since 2008 and provides all the data of this work. [36] All the information and data are available on the web and anybody can access them, using the tools given by Fermi. [41]

The reconstruction method and data set of Fermi LAT is improved regularly, improving the statistics, the systematic errors and the point source subtraction. The latest data set to date, called Pass 8, is used for this work. One of the most important steps in the treatment process is the selection of the events. Every photon measured is saved along with all its properties in a data file. Then this list is filtered to keep only the relevant observations. The filter can be based on the incoming direction, the energy or the time of observation, but also on the quality of the event reconstruction. This last cut can be critical. It will determine the chances that the measured event is in fact a gamma ray, and not some background noise polluting the data. The more strict the filter is, the less events are kept for analysis and the statistical errors increase. This work uses the CLEAN class recommended by the Fermi team for diffuse emission analysis. [41]

The main parameters of the selection can be found in Tab 2.1.

Parameter name	Parameter value	Description
Event class	256 (CLEAN)	Quality parameter. Varies the level of background noise.
Event type	3	Back+front event.
Time boundaries	INDEF	Selecting all events since beginning of observation.
Minimum energy (MeV)	58.4731	Minimum energy of the event.
Maximum energy (MeV)	513056	Maximum energy of the event.
zmax (degrees)	90	Maximum zenith angle to get rid of the Earth contaminations, as recommended by the LAT instrument team.

Table 2.1.: List of the main parameters used for data selection. The exact script can be found in the appendix 5.1.

Another important point is the creation of the exposure map. It tells how long the telescope spent observing a given part of the sky. After dividing the count map by the exposure, a flux map is obtained that does not depend on the observation time of particular regions. For example, if the telescope observed the galactic center ten times more often than the Orion nebula, there is no way to know at first if the higher counts in the GC is due to the longer exposition time or a higher flux from this region.

The goal of this work is to study the diffuse sources of gamma-rays from inside and outside the Milky Way. Of course, the LAT does not differentiate them from point source gamma-rays. This has to be done manually as the last step in the treatment process. A catalog of gamma ray point sources (3FGL) is available on-line on NASA website [42]. This catalog lists most of the known and identified point sources, along with their spectral shape and flux. This information can then be used to model the number of counts coming from point sources and their spatial and energetic distribution. To achieve this, the point sources properties must be combined with the instrument properties. The point source flux is multiplied by the LAT exposure time corresponding to its position. This flux must also pass through the instrument and its defaults will deform the initial shape of the source. For a point source, the final image obtained by the detector is the Point

Spread Function (PSF) of the telescope and is given with the Fermi tools. Every point source is convoluted by the PSF corresponding to the initial event selection, creating the final point source map as would be observed by the instrument. Once this model map is obtained, it is subtracted from the data to only keep the diffuse emission (see Fig. 2.1). Since the models are never perfect and all point sources are not listed, errors or anomalies in the observations can appear. Keeping the dataset up-to-date allows to use the latest catalogs and best reconstruction.

Once all the data treatment is done, a flux map of the entire sky in  $\text{counts}/\text{s}/\text{m}^2/\text{GeV}/\text{sr}$  is produced. The map is divided in bins of  $0.5 \times 0.5$  degrees on a Cartesian projection, also called cones. Every bin contains 30 logarithmic energy bins ranging from 60 MeV to 513 GeV with a 1.2 multiplicative step. Thus the final data cube is of dimension  $720 \times 360 \times 30$ . For visibility purposes, every energy bin is multiplied by its energy squared, becoming an energy flux in  $\text{GeV}/\text{s}/\text{m}^2/\text{sr}$ . This will be the default units used for the rest of this work.

The errors on the data are coming from two sources. First are systematic errors introduced by the instrument or the treatment process. They are around 3%, but can increase for low or high energies (Fig. 2.2). These errors have multiple causes, mainly the PSF and the energy resolution (or energy dispersion) of the instrument. The plot shows how the systematic errors vary when correcting, or not, for these effects. The treatment shown in appendix 5.1 accounts for energy dispersion. The second source is the statistical errors, proportional to the square root of counts. This property will make them decrease when the acquisition time will increase. They are dominant at high energy (above 50 GeV) where fewer events are observed. On contrary at low energies (around 100 MeV), the systematic errors dominate. The final equation is the following :

$$\sigma_{tot} = \sqrt{\sigma_{sys}^2 + \sigma_{stat}^2} = \sqrt{\sigma_{sys}^2 + \frac{1}{N}} \quad (2.1)$$

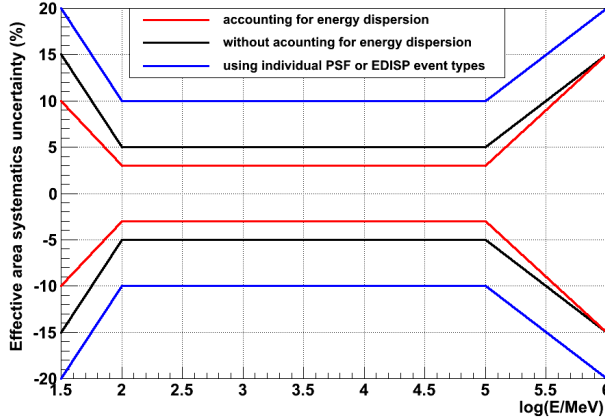


Figure 2.2.: Systematic error for Pass 8 data as a function of the energy and the treatment procedure. The energy dispersion is the energy resolution of the instrument; this effect is known and can be corrected (in red), lowering the systematic errors. This is what was done for this study. The black line does not account for energy dispersion. The blue line shows the systematics for specific event types, a treatment method that was not used for this work. The few percent gained with the energy dispersion treatment at very low energies (below a few hundred MeV), where the statistical uncertainties are not dominant any more, can be critical.

## 2.2. Model components

### 2.2.1. From CRs to gamma-rays

The gamma-ray spectra used in this study are directly calculated from the CR spectra. The next section describes the CR distribution used to get the gamma-ray spectra corresponding to the modeled processes. Once the CR spectrum is defined, a propagation software [43], DRAGON, is used to determine the emitted gamma-ray spectrum. For most of the components, the spectral shape does not vary depending on the direction, only its normalization does. DRAGON uses a model of the galaxy (ISRF, matter distribution, etc...) and the input CR spectra for protons and electrons to produce gamma-ray spectra as an output for pion decay, bremsstrahlung and inverse compton scattering.

### 2.2.2. Basic components

#### $\pi^0$ production by propagated cosmic rays (PCR)

The initial propagated proton spectrum for the PCR template is obtained from the observed proton data from AMS-02 [44]. A good approximation is an unbroken power law ( $R^{-\alpha}$ ) with a spectral index ( $\alpha$ ) of 2.85 at rigidities above 45 GV. At lower rigidities, the flux is not described by the power law because of solar modulations [45], as seen in Fig. 2.3a.

#### Inverse Compton (IC) and bremsstrahlung (BR)

The interstellar electron spectra need a break around 0.2 GeV with a spectral index of 3.21 above. This is compatible with the locally observed electron spectrum (see Fig.

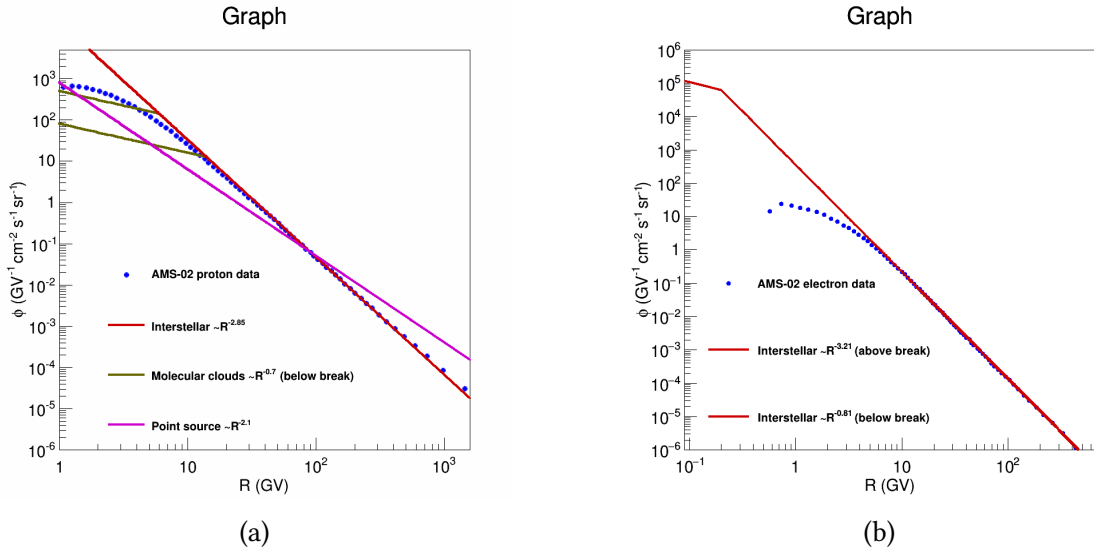


Figure 2.3.: Cosmic Ray spectra used to determine the gamma-ray templates. (a) Power-law proton spectra used to produce the proton based templates. In comparison, the measured data by AMS-02. The MC spectrum breaks are varying between the two shown here. Above the break, the index is the same than or propagated CR. (b) Power-law electron spectrum used to produce the IC and BR templates, compared once again with AMS-02 data. This time a break is introduced at 0.2 GeV.

2.3b). Below the break the optimal spectral index is 0.81, which implies a suppression of electrons. The targets for the production of gamma-rays are the interstellar gas for BR and the interstellar radiation field (IRF) for IC, which are both strongly dependent of position, so the photon composition varies with sky direction. For this reason, the IC and BR templates are calculated for each sky direction. The variation over the sky is about  $\pm 10\%$ , as shown in 2.4a. The BR template only depends on the interstellar gas distribution, decreasing the variations considerably compared to IC, as shown in 2.4b.

### 2.2.3. Additional components

#### $\pi^0$ production by source cosmic rays (SCR)

The proton spectra producing the SCR template can be described by a power law with a spectral index of 2.1, as obtained from the best gamma-ray template fit. The index 2.1 for the SCR template is expected from diffuse shock wave acceleration [46] [47]. The source CRs are accelerated and did not have time to escape the galaxy, hence a harder spectrum at high energies compared to propagated CR spectrum is expected.

#### $\pi^0$ production by molecular clouds cosmic rays (MCR)

A proton spectrum with broken power-law can be used to parameterize the decreasing gamma-ray emissivity from MCs below 2 GeV. The break can vary from 6 to 14 GeV for different clouds according to the fit. Above the break an optimal spectral index of 2.85 was found to be the same as for the PCR spectrum, as expected if the high energy propagated protons are above a certain magnetic cutoff. Below the break, the spectral index is 0.7, thus providing a significant suppression of protons below the break, as can

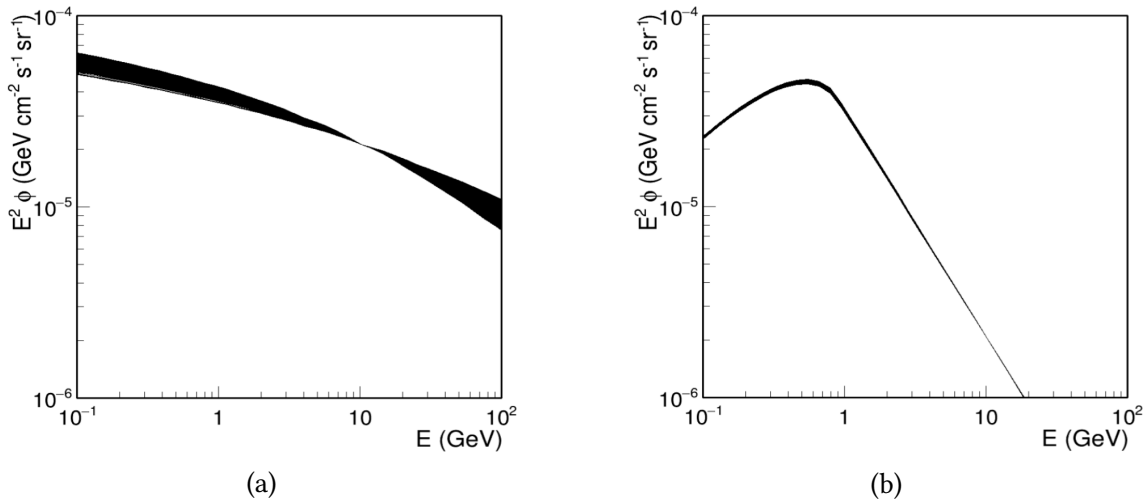


Figure 2.4.: (a): Superposition of the inverse compton scattering template in every sky direction, normalized arbitrarily at 10 GeV. (b): Superposition of the bremsstrahlung template in every sky direction, normalized at 10 GeV. The CR electron spectrum use here has a break at 1 GeV, but its position does not influence the spatial variations. The variations of BR are very small and can be neglected.

be seen from Fig. 2.3a. This lower break spectral index does not have a strong influence on the fit and therefore is taken to be 0.7. Variations in the magnetic cutoff in MCs are expected from the variations in size and in magnetic field, the latter increasing with MC density [27]. These variations, between 6 and 14 GeV, make the position of the gamma-ray spectrum maximum vary around a few GeV.

## Dark matter annihilation (DM)

Dark matter particles are expected to annihilate and produce hadrons of energies up to twice the WIMP mass, just like in electron-positron annihilation. This would be a large contribution to gamma-rays via  $\pi^0$  decays. A smaller fraction of WIMP annihilation can lead to  $\tau$  lepton pairs, which can lead to  $\pi^0$  production in the hadronic  $\tau$  decays. This contribution is expected to be small and is neglected. The DM template were calculated based on the DarkSusy software [48] [49]. An annihilation signal peaking around 2-3 GeV requires a WIMP mass around 50 GeV, as shown in Fig. 2.5b. The DM template falls down to zero for energies above twice the WIMP mass, which make it a softer spectrum than MCR.

## Milli-second pulsars gamma-ray production (MSP)

The MSP template is directly taken from the Fermi study [39]. It simulates the emission of 1700 millisecond pulsars with different energies around the galactic center. The high energy shape of the spectrum closely resemble the DM template, but the main difference with DM and MCR is for low energies. Indeed, below 1 GeV, the MSP template is a lot softer and this feature makes it discernible from MCR and DM.

## Isotropic component

The isotropic template represents the contribution from the isotropic extragalactic background and hadron mis-identification. Its spectral shape and absolute normalization are

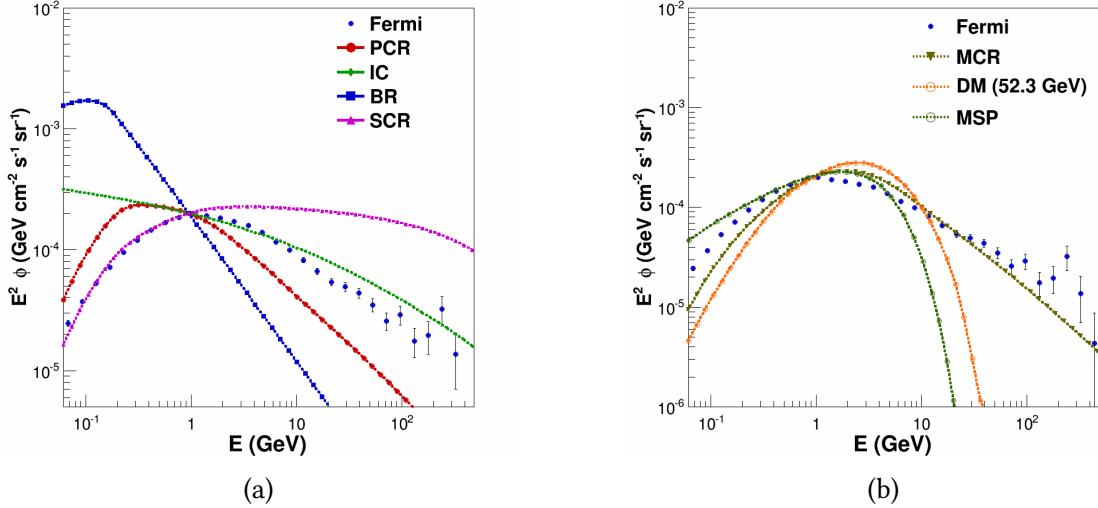


Figure 2.5.: (a) Comparison of PCR, IC, BR and SCR templates, normalized at 1 GeV. Measured data from the central molecular zone is shown as well. All four components have very different spectrum and index that make them easily identifiable by the fit. (b) Comparison of the three excess components, along with the data from the CMZ.

provided within the Fermi software [41], but it was redetermined for the analysis as follows. A first fit of the data in regions outside the bubbles and the galactic disk using the isotropic template from the Fermi software is produced as an initial estimate. This fit takes into account all components of the best fit available. If one plots the total observed gamma-ray flux versus the fitted flux in the various cones in a certain energy bin, one expects a linear relation crossing the origin if the isotropic flux is estimated correctly (See Fig. 2.6). However, if the isotropic contribution is either too low or too high, an offset at the origin is introduced in the linear relation. Since the isotropic component is by definition the same for all cones for a given energy, this offset can be subtracted from the Fermi template to improve the fit. Once the offset is determined for each energy bin and subtracted from the original template, the process is repeated until the offset converges to zero. This process is illustrated in its four first steps in the appendix A.1.

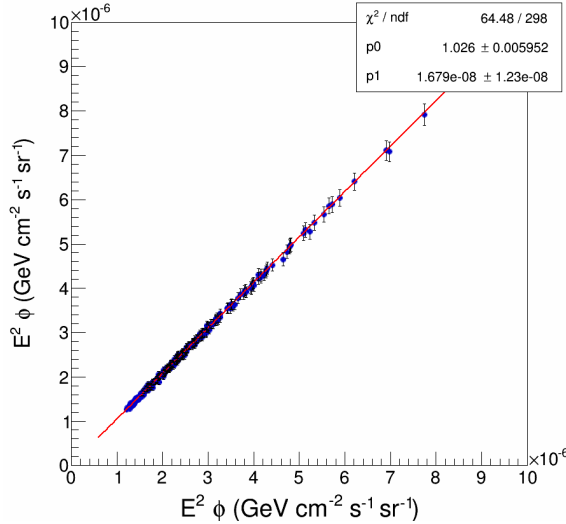


Figure 2.6.: The fitted flux versus the observed flux data in every region of the sky for a given energy of 1 GeV. A linear fit is performed to find the offset  $p_1$  at the vertical axis. This number represents the amount the isotropic component shifts the data in all cones. Once this is done for every energy bin, the offset is added to the previous isotropic template and the process is repeated until convergence.

## 2.3. Fitting method

The fitted data can be seen as a data cube whose dimension are longitude, latitude and energy. The finest spatial grid is divided in  $720 \times 360$  cones of  $0.5^\circ \times 0.5^\circ$ . Every cone contains 30 energy bins. This allows to treat different portions of the sky independently of one another. Since the cones do not have the same solid angle and the statistics in a small binning is low, the grid is sometimes composed of 797 bins of different sizes, bigger at the poles and smaller near the equator. This allows for higher statistics in lower flux regions and where a high spatial resolution is not needed (i.e. at high latitudes). In the same time, the equator and the GC have a lot more counts and can be treated in a smaller binning. This binning is faster to compute than a regular grid with an good enough output quality to study the results, nevertheless, most of the maps shown later use a one by one degree binning for the whole sky for aesthetic reasons.

The fit uses a certain number of components (three at least) each corresponding to a certain phenomenon and described earlier. They all have certain energy spectra that can vary with the position in the sky in the case of IC (See Fig. 2.5).

The fits are done for every bin independently. After choosing the templates used for the fit, their scaling factor is the only degree of freedom allowed. Using a ROOT TVirtualFitter object, every template is scaled up or down until its sum comes the closest to the data. So the modeled flux is given by:

$$\phi(E, l, b) = \sum_{i=1}^n a_i(l, b) * T_i(E, l, b) \quad (2.2)$$

where  $\phi(E, l, b)$  is the total fitted flux at energy  $E$ , longitude  $l$  and latitude  $b$ ,  $n$  is the number of components used in the fit,  $a_i(l, b)$  is the scaling factor of component  $i$  at

position  $(l, b)$  and  $T_i(E, l, b)$  is the  $i^{th}$  component's model flux. Only the IC and BR component depends on the longitude and latitude, and the isotropic template has a fixed scaling factor.

Mathematically, the minimum distance between the model and the data is found when the  $\chi^2$  value is lowest. It is calculated as follows:

$$\chi^2 = \sum_{i=1}^{30} \left[ \frac{(D_i - \sum_{j=1}^n [(a_j T_{ij})^2] + iso)^2}{\sigma_i^2} \right] \quad (2.3)$$

where:

- $D_i$  is the data flux in the  $i^{th}$  energy bin.
- $a_j$  is the scaling factor for the  $j^{th}$  model component.
- $T_{ij}$  is the model flux of the  $j^{th}$  in the  $i^{th}$  energy bin.
- $\sigma_i$  is the geometric mean of the statistical and systematical error of the Fermi data point  $i$ .

The MCR break position does not vary in a single fit. A fit is done for different values of the MCR break independently, and the one with the smallest  $\chi^2$  is kept. This break position is not counted as a degree of freedom in the fit.

The fit is very well constrained with only five or six degrees of freedoms depending on the model against 30 data points. A useful value is the  $\chi^2/d.o.f$  where  $d.o.f = \#data\ points - \#free\ parameters - 1$ . Thus, if a model describes data completely within its uncertainty,  $\chi^2/d.o.f = 1$ , making the comparison between different fits easier. This rescaling will be applied every time when speaking about  $\chi^2$  in the rest of the discussion, except if explicitly told. The closer a  $\chi^2$  value is to one, the better the model follows the data. The higher it gets, the lower the quality of the fit. It can also happen that it gets lower than one. This can happen when the error bars on the data are too big.

Since every bin is fitted independently, it is not possible to implement a spatial template, i.e. where the spatial shape of a component would be fixed in advance. For example a component with a spherical distribution around the GC, as has been done in other works [38], [50]. It is used to let the fit find reasonable shapes by itself, only using the  $\chi^2$  minimization technique.

This fitting method offers many ways to look at the results, depending on the interest. It is possible to produce flux maps of each component to study their spatial shapes at different energies. This can for example show a correlation between a certain template and a galactic feature such as the disk or the bubbles. Another way is to create a spectrum of one cone to look at the relative quantity of every template at different energies. This can put into evidence issues within the models and help improve the spectral shape of the components.

The first step when testing a new model is to see if it can reproduce results of previous studies. Only once it works and can be confidently used, can it produce new results.



### 3. First results: Study of the excess

#### 3.1. Recreating previous results

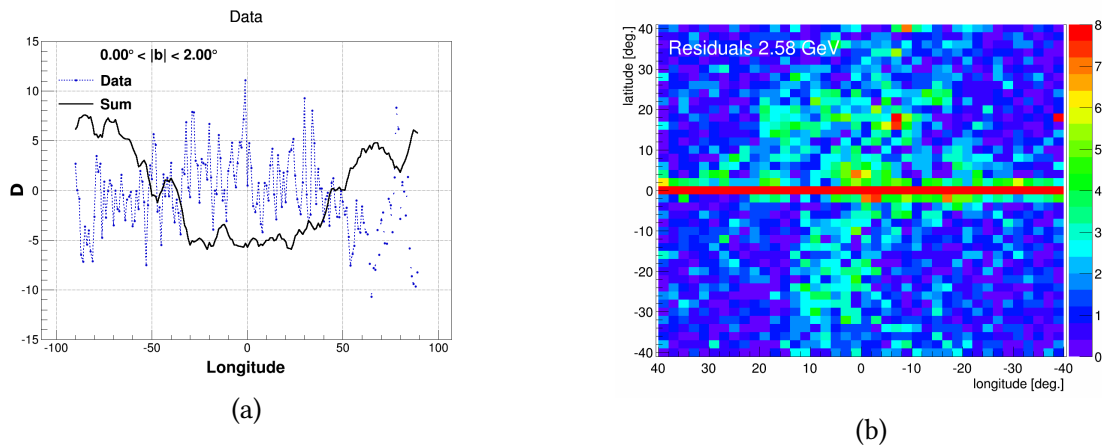


Figure 3.1.: Representation of the GC excess. (a) Scaled difference (eq. 3.1) in the Fermi data flux between 300 MeV and 2 GeV for all longitudes below 2 degrees in latitudes (in blue). The peak in the GC indicates a harder spectrum that traces the excess. Following the same equation, the fitted background model (in black) do not show the same shape. The index of the model is clearly not high enough around the GC. (b) Map around the GC of the difference in percent between the model and the data at 2 GeV. The disk is very problematic, but the interesting feature is the more or less spherical shape around it. The difference decreases as the distance from the GC increases.

Before trying to upgrade the current model, it is important to make sure it can be recreated with this method.

3.1a illustrate a way of seeing the excess, without using any fit method, only the data. For absolute latitudes below two degrees, the difference  $D$  of the Fermi data between 5 GeV and 300 MeV is plotted for all longitudes. For every sky direction,  $D$  is given by equation 3.1.

$$D = \frac{(Data(E_1, l, b) - Data(E_2, l, b))}{\sqrt{\sigma_{1, stat}^2 + \sigma_{2, stat}^2}} \quad (3.1)$$

where  $Data(E_i, l, b)$  is the Fermi flux at energy  $E_i$ , longitude  $l$ , latitude  $b$ , and  $\sigma_{i, stat}$  is the statistical uncertainties on the Fermi flux at energy  $E_i$ .

It is then scaled around zero for visibility. A peak is dominating in the center, indicating an increase in the spectrum index. This can be interpreted as the excess component rising and changing the shape of the spectrum.

Fig. 3.1b presents an other way of looking at the excess with a fit using only the background components (PCR, IC and BR). This map shows the relative difference between the fit and the data at 2.58 GeV. This gives an idea about the distribution of the excess around the GC. The shape and intensity of the previously observed excess are found [51]. Excluding the galactic disk for latitudes below two degrees, the excess extends to  $30^\circ$  in all directions from the GC. The problem continues to arise when looking deeper into the results.

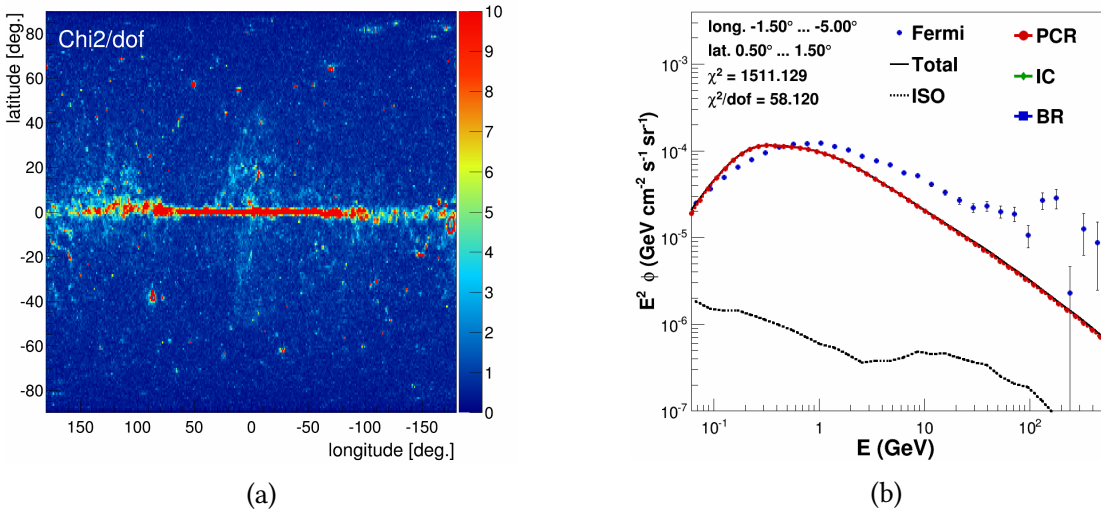


Figure 3.2.: (a) Spectrum of the CMZ region and its fit using only the three background components (the IC and BR contributions are too low to be seen on this graph). Two major problems can be identified. First a hardening of the spectrum above 10 GeV; second the shift of the spectrum maximum between the model and the Fermi data. (b) The best  $\chi^2$  value obtained by the fit for every sky direction. The bubbles structures and the galactic disk are visible, with a very large disagreement between the model and the data. These bad  $\chi^2$  regions are the sign that one or two of the problems identified on the left are present. Several bad spots can also be identified. These correspond to a bad point source subtraction when processing the data (cf. chapter 2) and should be ignored.

Looking at the  $\chi^2$  distribution on the sky (Fig. 3.2a), the bubbles and the disk appear clearly in red, showing a high  $\chi^2$  value. The fit does not give proper results in those regions, with the high energy part of the spectrum not described by the three background

templates as shown by Figure 3.2b. This example spectrum from the galactic center illustrates the two main challenges. First, the high energy tail of the data is not compatible with the model, much higher and with a harder spectral index. The second problem is the shift in the peak position. The data peaks around one or two GeV when the model peaks only around a few hundred MeV. These two differences are investigated in more detail in the following sections. Outside these regions, the fit works a lot better, with a  $\chi^2$  not much bigger than three. This is not perfect, but in comparison with the disk, the model describes the data better.

### 3.1.1. EGRET Data

One of the previous gamma-ray space telescope called the Energetic Gamma Ray Experiment Telescope (EGRET) [37] gave a first insight on the GC excess. Its energy range did not exceed 30 GeV, and the data overall quality is worse than that of the LAT. It is a good way to compare the results. A model for DM was fitted on the EGRET data to test the hypothesis [52]. Figure 3.3a and 3.3b compares the results of this study to the previous study. For a large region around the GC, the Fermi and EGRET data were fitted with a PCR, IC, BR and DM template. The WIMP mass is 40 GeV and the fit only considers points below 10 GeV, even if it shows the higher energies as well, to be consistent for both studies. It is a first attempt to recreate previous results with an excess component. When the fit works perfectly for the EGRET data on the left, a clear deficit can be observed for Fermi data. Above 10 GeV, EGRET has no data and the shape could lead to believe that a rapid drop occurs. But Fermi does not show this drop, and present a harder spectrum than what could be expected from EGRET data. The difference is all in this hard high energy tail. It shows that even if the first measurements could be fitted by adding a single excess component like DM, it is not possible with Fermi data: the addition of a new component with a very hard spectrum is necessary. This is done with the introduction of the SCR component.

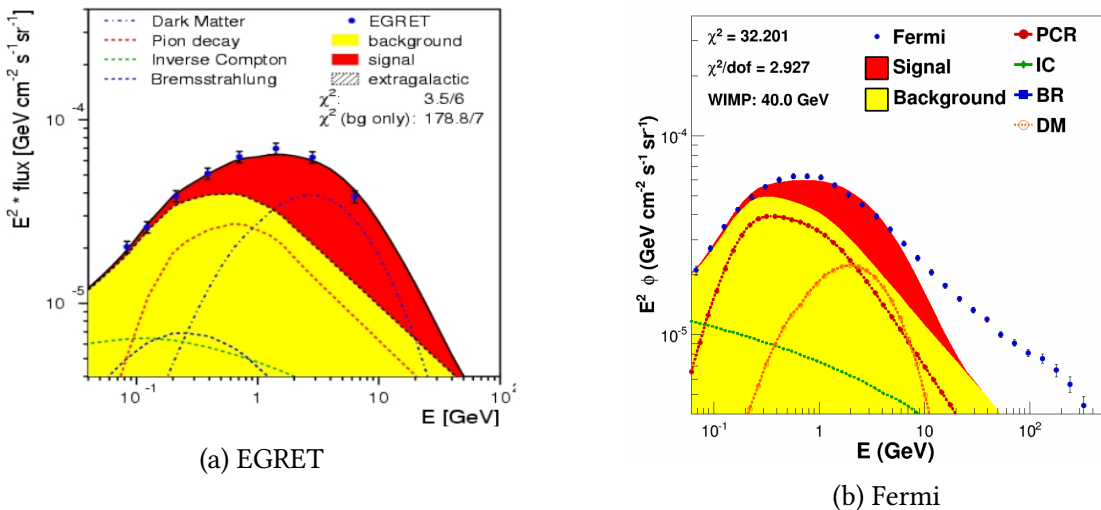


Figure 3.3.: Comparison of the EGRET (a) and Fermi (b) data with the model. The EGRET data were fitted by [52], and their model take a PCR, BR, IC and dark matter templates. The maximum energy of the EGRET data is 10 GeV, and the model agrees relatively well at all energies. The model used on the Fermi data is as close as possible from the EGRET model, with the PCR, BR, IC and DM template as described in Chapter 2, but this time the data go up to 500 GeV. Once again, the model agrees for all energies below 10 GeV; but it can not account for the energies above. This is an indication that high energies are harder than expected and require the addition of a new component to the model.

## 3.2. Introducing SCR

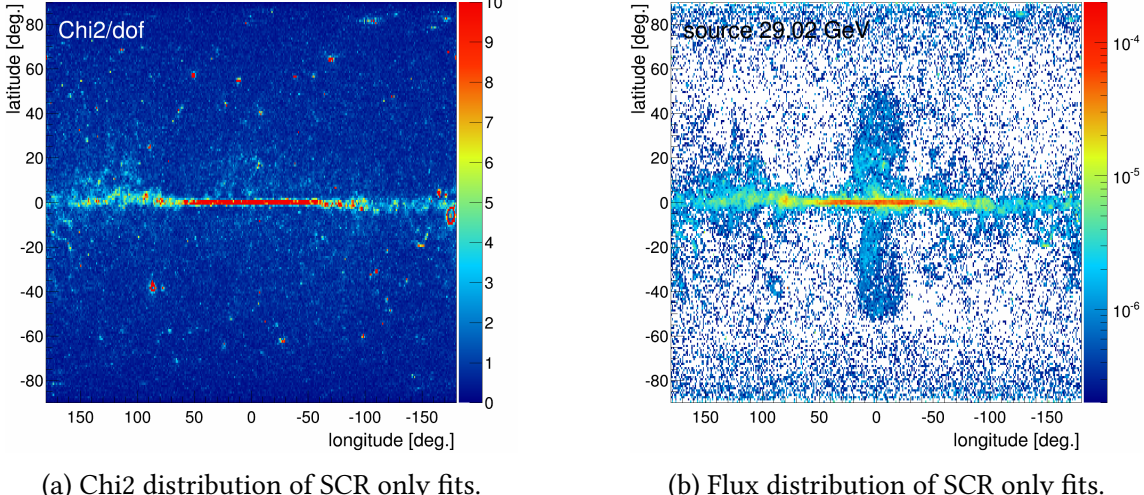


Figure 3.4.: Results of fit including the SCR component. (a)  $\chi^2$  distribution. The bubbles are not so clear than before, but the disk is still visible (cf Fig. 3.2a). (b) Flux distribution of the SCR template at 30 GeV. The bubbles and the disk are distinct. The SCR template traces the hardening in the data high energy spectrum, thus showing it here. This distribution was expected, in the bubbles because of unpropagated proton CR ejected from the GC, and in the disk because of point sources that are not subtracted.

A fourth component is needed to fit the data in the disk and the bubbles in addition to the basic templates. This is due to a hardening of the spectrum at high energy that is thought to be induced by non propagated CR, i.e. CR that do not propagate through dense gas clouds or highly convoluted magnetic fields. For example in the bubbles, where particles are ejected without passing through dust clouds; or simply near sources, where CR do not have time to interact with the interstellar medium.

After introducing the SCR template, a clear improvement can be noted in the  $\chi^2$  distribution (comparing Fig. 3.4a to Fig. 3.2a). The bubble shape that was delimited before by a bad  $\chi^2$  zone has now disappeared. Even if the fit is still not perfect everywhere, the improvement is significant. The disk is still not fitted properly, with very high  $\chi^2$  values, over 10. Some structures can also be seen along the disk for absolute longitudes over  $90^\circ$ . These remaining bad fits tend to show that the model is still not fully described yet, and could be improved, as seen in following sections.

The SCR template is present only in the disk and the bubbles (see Fig. 3.4b), as expected. The map of fitted SCR component shows it clearly, delimiting the bubbles with great precision. This distribution reinforces the idea of a source component, by pointing to all the regions where a hardening of the spectrum is present, as expected from its physical interpretation. It also does not disrupt the other components distribution too much. The PCR, IC and BR distributions are similar and still match their expected shape (Appendix B.2 and B.3).

Figure 3.5 shows the spectrum in a given direction inside the bubbles, before and after adding the SCR template. While the high energy parts (above 100 GeV) of the spectra are

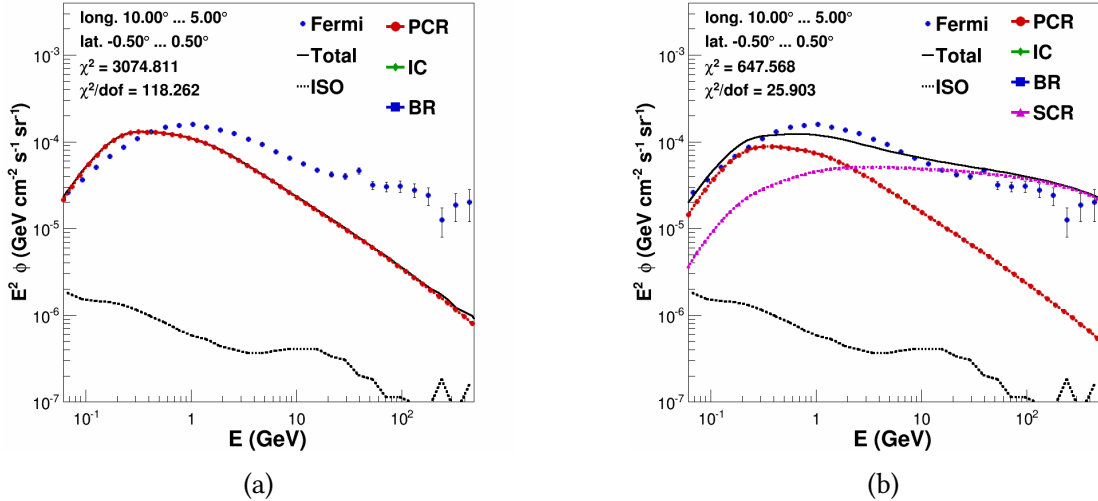


Figure 3.5.: (a) Fit results in the direction of a bubble using only the three background templates. The problems identified before are here, with a hard high energy tail and a slight shift in the maximum position. (b) Fit results in the direction of a bubble using only the three background and the SCR template. This time, the small shift is still present, but the high energy hardening is fitted by the SCR template.

dominated by SCR, the lower energies are also fitted with PCR. The major difference is that each template fit one part of the spectrum, leaving other component deal with the rest. SCR is present at high energies, and this leaves more room for PCR to adapt to the low energy spectrum. Hence increasing the fit quality.

This four-template fit represent a clear improvement compared to the background only (PCR, IC and BR) model. But, as seen on the  $\chi^2$  distribution map (Fig. 3.4a), the disk and low latitudes regions are still not fitted properly. Figure 3.6b shows it well. The PCR spectrum does not peak at the right energy. The Fermi data has its maximum around a few GeV, while PCR's is only at a few hundred MeV. This problem leads to a very high contribution of SCR, trying to fit the data's maximum and the high energies at the same time; task that can not be done with SCR's spectral shape. This leads to the introduction of the first excess component, added to solve this problem.

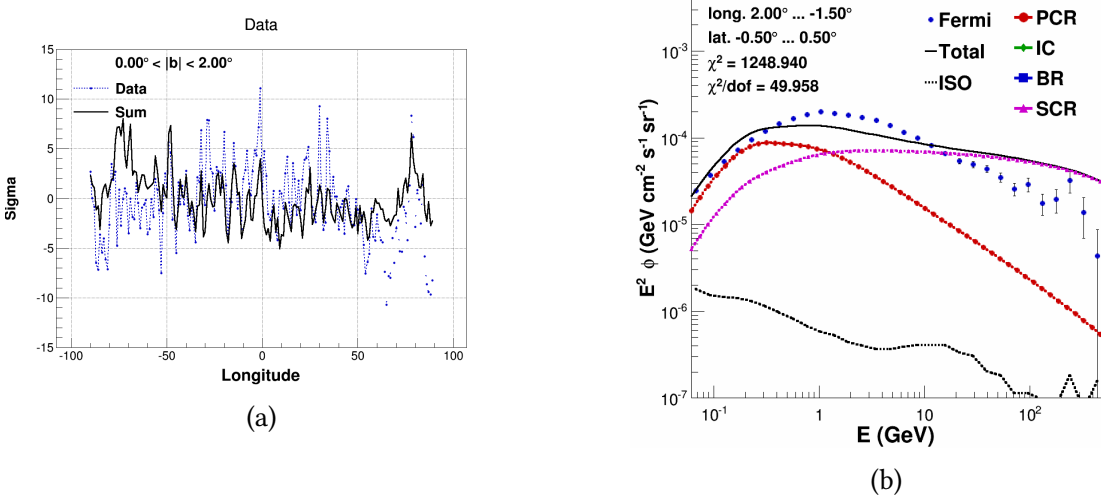


Figure 3.6.: (a) Approximation of the Fermi data index (in blue) between 300 MeV and 2 GeV for all longitudes below 2 degrees in latitudes. In comparison the fitted background model with SCR (in black). Comparing to Fig. 3.1a an improvement can be noted, even if model does not follow the data. (b) Spectrum from the GC, where the excess is supposed to be the highest. The SCR component overshoot the high energies to compensate a lack of gamma ray flux at 2 GeV. But introducing an excess component should cover the lack and the SCR contribution should decrease everywhere the 2 GeV excess is present.

### 3.3. Introducing an excess component

#### 3.3.1. Introducing MCR

As shown on Fig. B.4a, the addition of the new MCR template improves significantly the  $\chi^2$  distribution in all directions. The bubbles and the disk structures are not visible any more. Such a flat distribution is one of the best indicator of a good fit. Three red dots appear to have a really high  $\chi^2$ , but that is only due to the point source subtraction that is not perfect (see Chapter 2.1). This direction can be identified on almost every fit done in this paper, and should not be taken into account too seriously for the analysis.

Fig. 3.7a shows the central molecular zone (CMZ) fitted with the MCR component. The gas density is very high in this region, hence it is the first region where we would expect the MCR emission to be present. Indeed the fit chooses a configuration where the MCR template is dominating all the others and directly improving the fit compared to Fig. 3.6b. The energies around 2 GeV had a clear excess that the four components of the SCR fit could not account for. The MCR template peaking in this region, it comes in very handy and fill this gap, leaving the SCR template taking care of the high energies and the background components for the lower energies. Fig. 3.7b can be compared to Fig. 3.1a and 3.6a. This time, the model follows the data almost perfectly, and marks every peak. This clearly shows the improvement of the fit at low energies, and the positive effect of the new excess component.

Then, looking at the spatial distribution of the MCR template on figure 3.8b, it can be observed that the flux directly traces the CO emission map (Fig. 3.8a). CO being a tracer of MCs in the galaxy, the new excess template is linked to MCs as well.

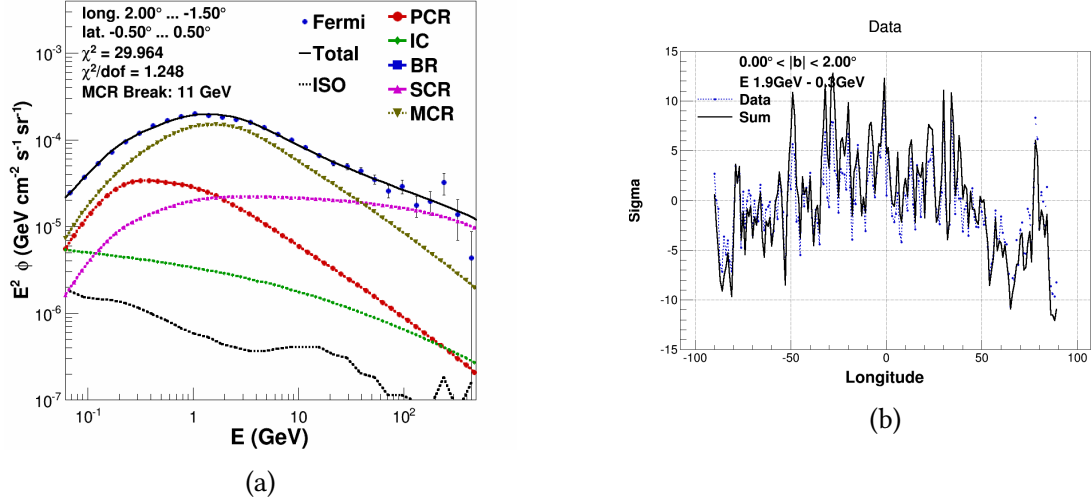


Figure 3.7.: (a) Approximation of the Fermi data index (in blue) between 300 MeV and 2 GeV for all longitudes below 2 degrees in latitudes. In comparison the fitted background model with SCR and MCR (in black). Comparing to Fig. 3.1a and Fig 3.6a an improvement can be noted and the model does follow the data. (b) Fit of the CMZ with PCR, BR, IC, SCR and MCR. The MCR template dominate all the other around 2 GeV, and allow a very low  $\chi^2$  value. Compared to Fig. 3.6b, the SCR component does not overshoot the high energies.

### 3.3.2. Introducing DM

Fitting the DM template instead of MCR requires a little more preparation. The first step is to determine which mass for the WIMP particles would produce the best spectrum for our fit. Fig. B.4d shows the best fit for the CMZ region, with the WIMP mass as a free parameter. This region was chosen to determine the mass because the excess is supposed to dominate the emission. Once the optimum mass for this direction is found, it is fixed and the fit is repeated in the entire sky. The fit chooses a mass of 52.3 GeV, peaking around a few GeV, as expected in from the excess position. Once the mass is determined and applied to the entire sky, the fit gives the following results. The  $\chi^2$  distribution (Fig. B.4c) is comparable to the MCR fit (Fig. B.4a) for the major part but is significantly worst in the disk. This effect would tend to indicate that a DM spectrum is less appropriate to describe the excess, even if nothing can be concluded yet.

Figure B.4d shows the fit of the CMZ using the DM component as the excess component. A first comparison with the MCR fit points to differences in the higher part of the spectrum. DM is way softer above 10 GeV and this change induces all the differences.

As seen on Fig. 3.8c, the DM distribution of the fit traces closely the distribution of molecular gas distribution (as traced by CO). The DM distribution resemble closely the MCR distribution obtained in the previous section (Fig. 3.8b). Looking at Fig. 3.9a, the same remark can be made, the model follows closely the data, as obtained for the MCR fit on Fig. 3.7b.

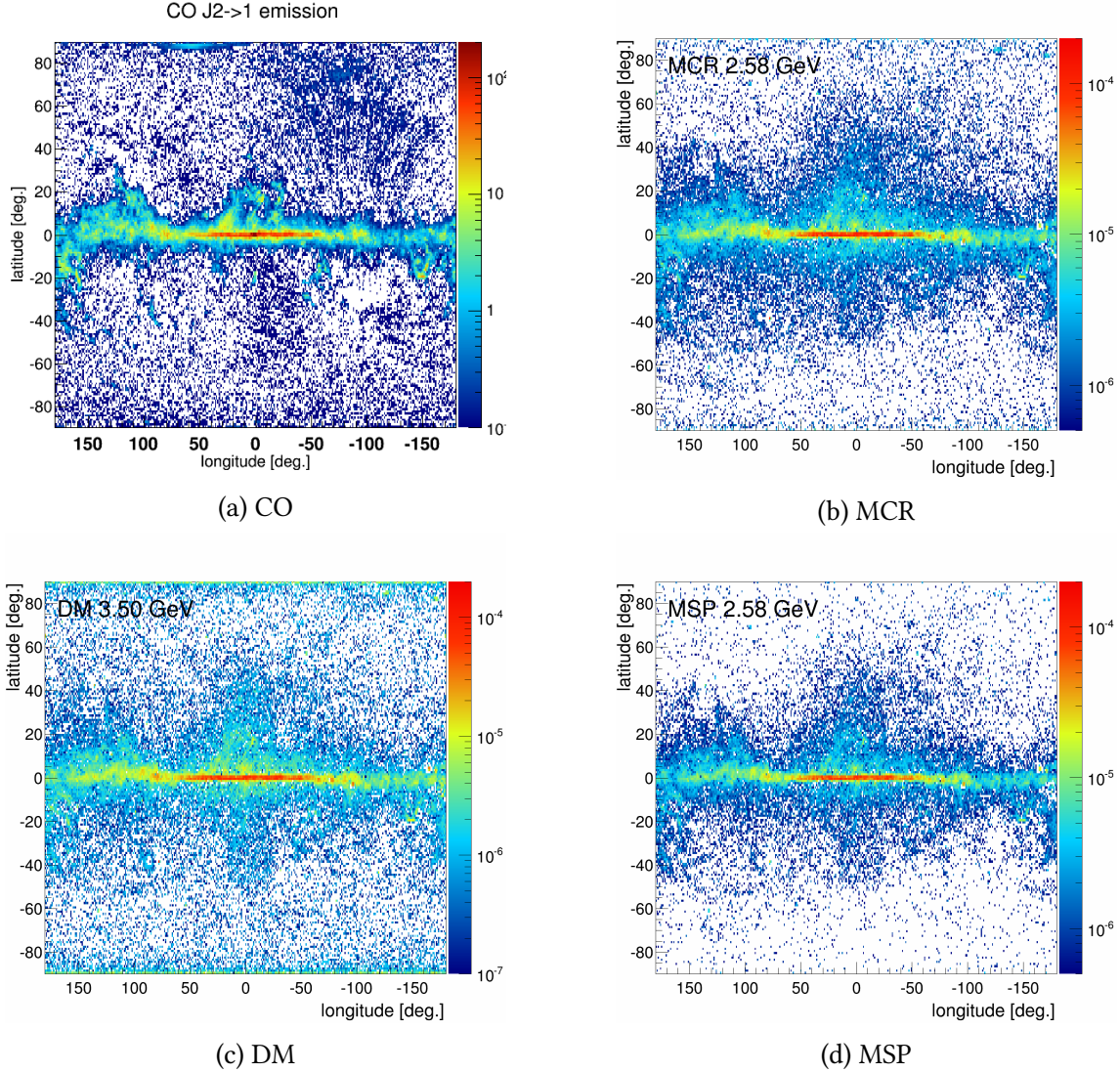


Figure 3.8.: Spatial distribution of the flux for CO (a), MCR (b), DM (c) and MSP (d).

The same structures appear in all four maps, with the disk clearly delimited between -90 and 90 degrees in longitude and a widening around the GC and 120 degrees in longitude. The distribution of molecular clouds as traced by CO can be found in the excess component distribution, whatever hypothesis is used. This is expected only for the MCR hypothesis, but not for DM or MSP.

### 3.3.3. Introducing MSP

This section introduces the results of the MSP as the excess component. The first thing that can be noticed when seeing the  $\chi^2$  distribution of the MSP only fit (Fig B.4e) is the similitude with the DM only fit (Fig. B.4c). The fit succeeds pretty well outside the disk, but gets significantly worst for latitudes below two degrees.

Using the MSP spectrum predicted by fermi [39] to fit the CMZ region does not give entire satisfaction. As for DM, the high energy is again too soft and put constraints on other templates.

As shown on Fig. 3.8d, the distribution of MSP in the sky resembles the distribution of CO, MCR and DM obtained in previous sections. Present everywhere in the disk, with a higher flux in GC and the bubbles. This statement is consolidated by figure 3.9b where we see that the model follows again the data almost perfectly.

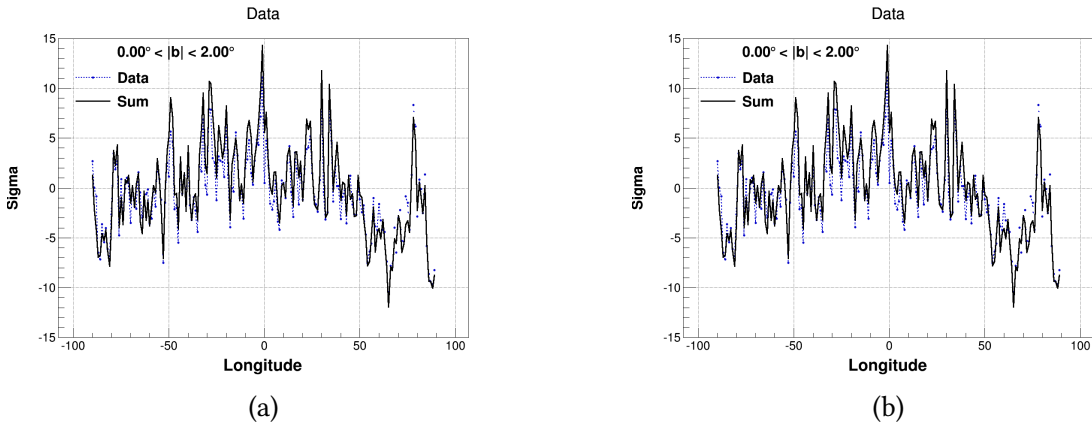


Figure 3.9.: (a) Approximation of the Fermi data index (in blue) between 300 MeV and 2 GeV for all longitudes below 2 degrees in latitudes. In comparison the fitted model with SCR and DM (in black). (b) Same graph but with MSP instead of DM.

### 3.4. Discussion on previous results

Gathering the results of the previous section, a conclusion tends to emerge: all three templates are similar and the results do not show big differences, but their interpretation might prefers the MCR hypothesis over DM and MSP. We will discuss why in this section.

A first step in understanding what is going on can be to compare the  $\chi^2$  skymaps. The higher is the  $\chi^2$ , the worst is the fit. Looking at the background only fit (with PCR, IC and BR only), the disk and the bubbles clearly define a bad  $\chi^2$  zone (as seen on Fig. 3.2a). The high energies are not described at all, with a fitted flux too low (see Fig. 3.5b). It indicates a lack of high energy components that could be able to bring a high energy contribution. This problem is solved by introducing the SCR component and does not play a major role in identifying the excess.

The first results with SCR added to the three background component is a success with clear improvement in the bubbles. They are not visible anymore when looking only at the  $\chi^2$  skymap and this is a very good sign. On the other hand, the disk is still not fitted correctly, as can be seen from the large  $\chi^2$  band at latitudes below a few degrees. Even if there is a small improvement, the addition of a fifth component can be beneficial. Now that the high energies are taken care of, the excess shows around a few GeV. There are three different candidates for the job: MCR, DM and MSP. All three correspond to a unique process with clear definitions and expectations.

The first hypothesis to be proposed for this excess was the presence of DM in the GC. As explained before, the DM halo is expected to be spherical around the GC following a NFW profile, since it does not interact with matter. And since the gamma-ray production from DM is directly proportional to the DM density, the DM component is expected to be spherical around the GC as well. There is no reasons for it to be correlated with the spatial shape of the Milky Way. But looking at the results (Fig. 3.8c), the fit does not meet these theoretical expectations for DM distribution. The DM flux follows the bar shape of the galaxy, with a high flux below two degrees in latitude and ninety degrees in longitude. Then, some distinct objects can be identified in the disk, around -90 and 90 degrees in longitudes. The MSP fit, also expected to have a spherical distribution of gamma-rays from millisecond pulsars, gives similar results. The flux seems to be needed by the fit to describe the disk and regions with molecular clouds as traced by CO in general. In both cases, the  $\chi^2$  maps show an improvement of the model, but the morphology of the new components tends to disagree with the theory.

The addition of MCR leads once again to the same kind of results, but this time, the spatial distribution is expected to follow the MCs. The  $\chi^2$  map is a little better than for the other two with the disappearance of the remaining bad fits in the disk. A  $\chi^2$  around one is obtain on the entire sky. The fact that this distribution tends to be the same for all three additional component could be expected, since their energy spectra are similar, and the excess they are supposed to describe has a fixed distribution. But the interesting point is that no spherical distribution is ever observed, nor needed, to fill the 2 GeV excess. The only differences in the models for the three excess component is the way theory and results matches. For DM and MSP, the results do not correspond to the predictions, when, on the contrary, MCR theory predicts the obtained morphology.

This quick comparison of the excess component distributions and the  $\chi^2$  maps gives a good overview of the results. But even if a preference for MCR can start to emerge, further investigation is preferable before being able to conclude.

### 3.4.1. Detailed comparison of the excess spectral shape

The only difference between the three excess components that the fit cares about is their spectral shape. It is explained in the chapter 2 that all three templates peak around 2 GeV, but the slopes at low or high energies are different. For energies inferior to 2 GeV, MCR and DM have a similar shape, when MSP is much softer. For energies above 2 GeV, it is the MSP and DM spectrum that look alike, with a very soft spectrum, when MCR is harder.

These differences are the only reasons the fits does not give exactly the same results three times. Indeed, the low energy spectrum of Fermi data in the disk is relatively hard compared to high latitudes. This plays a major role in differentiating MSP on one side, and MCR and DM on the other. The MSP spectrum being softer than Fermi at low energies, the lowest Fermi data point is limiting the MSP contribution. And the relative contribution of the MSP at 2 GeV can not exceed a certain value due to this soft energy spectrum. On the other hand, the MCR and DM spectra fall down with the same index than the data. Thus, the limit on MCR and DM relative contribution is not as limited by low energies as it is for MSP. This spectral particularity keeps MSP low and does not allow it to account completely for the excess in the GC.

On the other side of the spectrum, above 2 GeV, it is MCR that behave differently than MSP and DM with a harder spectrum. When DM and MSP are completely insignificant above 50 GeV, MCR still plays a role at least as important as the PCR spectrum since they both have the same spectra at high energies. Above 4 GeV, the Fermi data present an constant spectral index with very little variations in the disk. This makes all the difference to distinguish between MCR and MSP or DM. In fact, the important point here is the energy at which the SCR component cross the excess component. In the CMZ, this turnover happens at 50 GeV for MCR, against only 10 GeV and 6 GeV for DM and MSP respectively. This causes the total flux in the DM and MSP fits to present a dip around 11 GeV with a clear change in spectral index. This does not follow the shape of the data. Because of this, the SCR has to overshoot the very high energies (above 100 GeV), to minimize the size of the dip. The PCR component could be a good help with a constant spectral index at high energies, but its contribution is limited by low energies. Indeed, the PCR spectrum peaks around 200 MeV where the Fermi data are already decreasing rapidly. Overall, the MCR spectrum presents the right shape at high energies, with a constant spectral index hard enough to combine with the SCR component and closely follow the data.

In total, two major differences in the spectral shape of the three excess components could be enough to predict the most adapted one. The low energy spectral index difference between the MSP and the Fermi data leaves the MSP behind the MCR and DM hypothesis. Furthermore, the harder spectrum of MCR at high energies improve the fit significantly compared to MSP and DM. So the only spectrum that presents the right shape at low and high energies is MCR, making him the best candidates for a good model.

### 3.5. Correlation between the excess and molecular clouds

Plotting the spatial distribution of the excess component around the GC, and comparing it to the CO map of the galaxy is insightful. Figure 3.10 illustrates the correlation existing between molecular clouds as traced by CO emission and the MCR template. Several features can be identified by eye and found in both flux distributions. It is even clearer when plotting the CO flux versus the MCR flux, a linear correlation appears in the whole disk. Appendix B.5 shows the same correlation the DM and the MSP component. This once again favors MCR over DM or MSP, since only the first is supposed to follow the molecular clouds distribution.

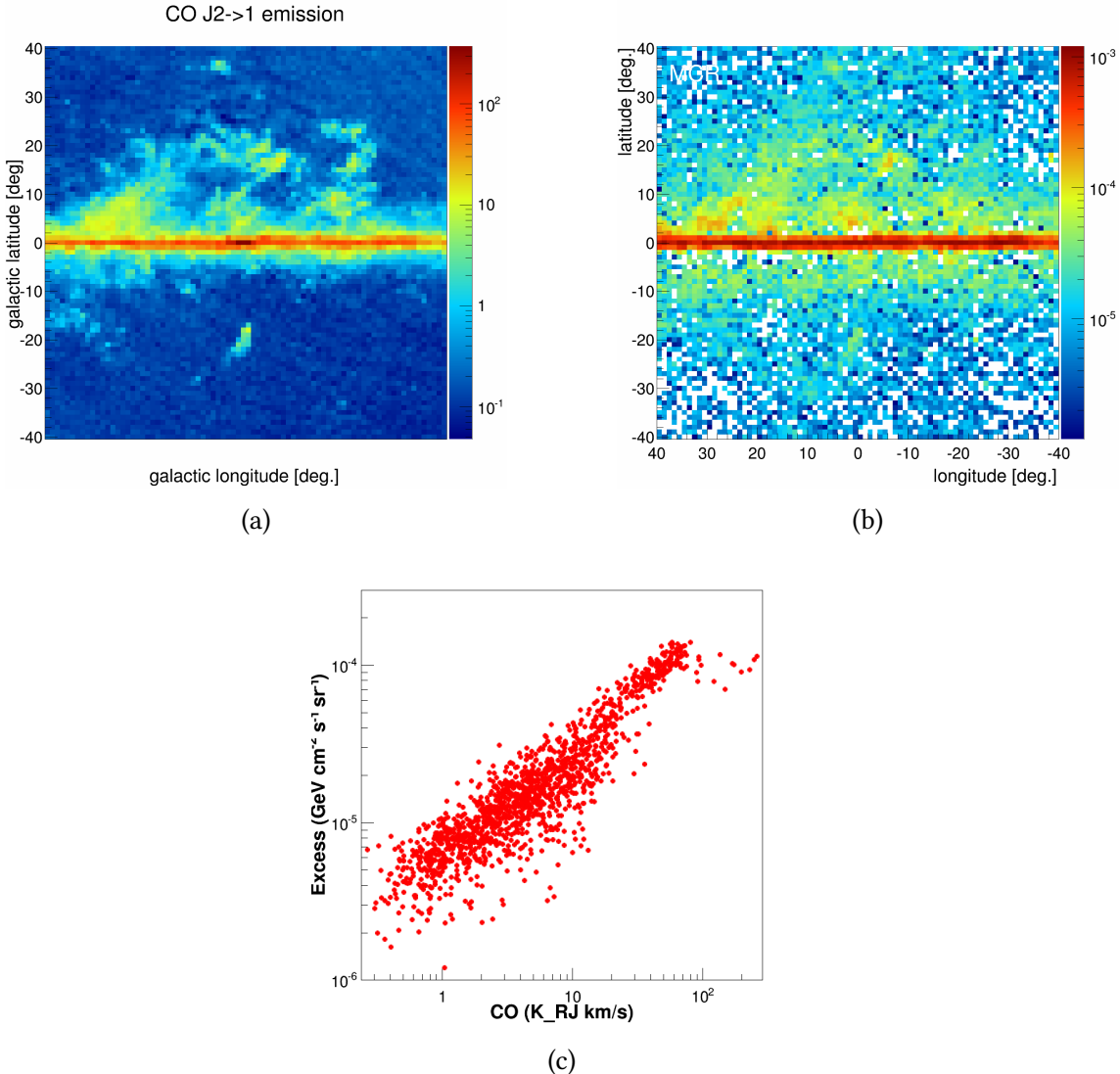


Figure 3.10.: (a) CO emission map around the GC. Molecular clouds follow the disk and show some features above. (b) MCR flux distribution as obtained by the fit around the GC. The disk and several features are very similar to the CO map. (c) CO flux versus MCR flux in every cones of the disk below two degrees latitude. A very clear correlation can be observed, linking the excess component to the molecular clouds.



## **4. To go further: How to improve the model**

### **4.1. Discussion on the spatial distributions of the other components.**

The spatial distribution of a component can teach a lot about the fit. Every component is closely linked to a known physical process taking place in the Milky way. So even if the components contributions to a single cone can not be predicted, large scale structures should emerge and coincide with the predictions. Using this, it is possible to verify the proper functioning of the fit by comparing the fitted spatial distribution of the different templates and the predicted one. For example, the distribution of the ISRF is expected to be spherical around the GC in the UV range, where most of the starlight is emitted. It can also follow the dust distribution in the disk in the infra-red range. This can be used to check if the IC component is coherent in the fit and follows, to some extent, the ISRF distribution. Hopefully, the results show a spherical IC component centred on the GC. The different distributions of each component will be discussed in the following section.

#### **4.1.1. PCR flux distribution**

The PCR component is produced by diffuse CR protons which collide with other hadrons and form a neutral pion, which in turn decays into two photons. So the PCR flux is directly proportional to diffuse CR, gas and dust density in the galaxy along the line of sight. It is expected to be present in every direction, with a stronger flux coming from the disc, and less from high latitudes. The bubbles have a harder CR proton spectrum composed of source protons. This implies that more high energy pions are created in those regions, and the PCR flux should be more important. However, this is not the case because of the presence of the SCR component. The latter was created specifically for such regions with a hard CR spectrum and should take care of them instead of PCR. This way, PCR should not follow the bubble shapes.

The results are very similar for the three fits, with MCR, DM or MSP (Fig. 4.1). The galactic disk is clearly visible at all longitudes, up to twenty degrees in latitude. Some

structures from the gamma ray sky are also here, with the bulge around the GC and diffuse shapes at the anti-center. Looking carefully at the disk below two degrees in latitude near the GC, the flux decreases a little, when it is supposed to be the highest. Indeed, the GC is where the density of matter along the line of sight is the most important, and so PCR should follow it. This gap structure could be interpreted as the result of a higher concentration of molecular clouds in this area, cutting off low energy CR, as modeled by MCR. This effect could affect the proportion of PCR gamma-rays in favor of MCR and reverse the relative contributions. Thus MCR should replace PCR, but the sum of both components should still show an increase in flux toward the GC. Indeed, the sum skymaps is coherent (see appendix C.6). Like for the bubbles, the propagated proton CR spectrum changes too much in different environments to be described by a single power law. If this interpretation is correct and is not just a fitting mistake, it is another argument that can easily be explained by the MCR hypothesis, but not by DM or MSP.

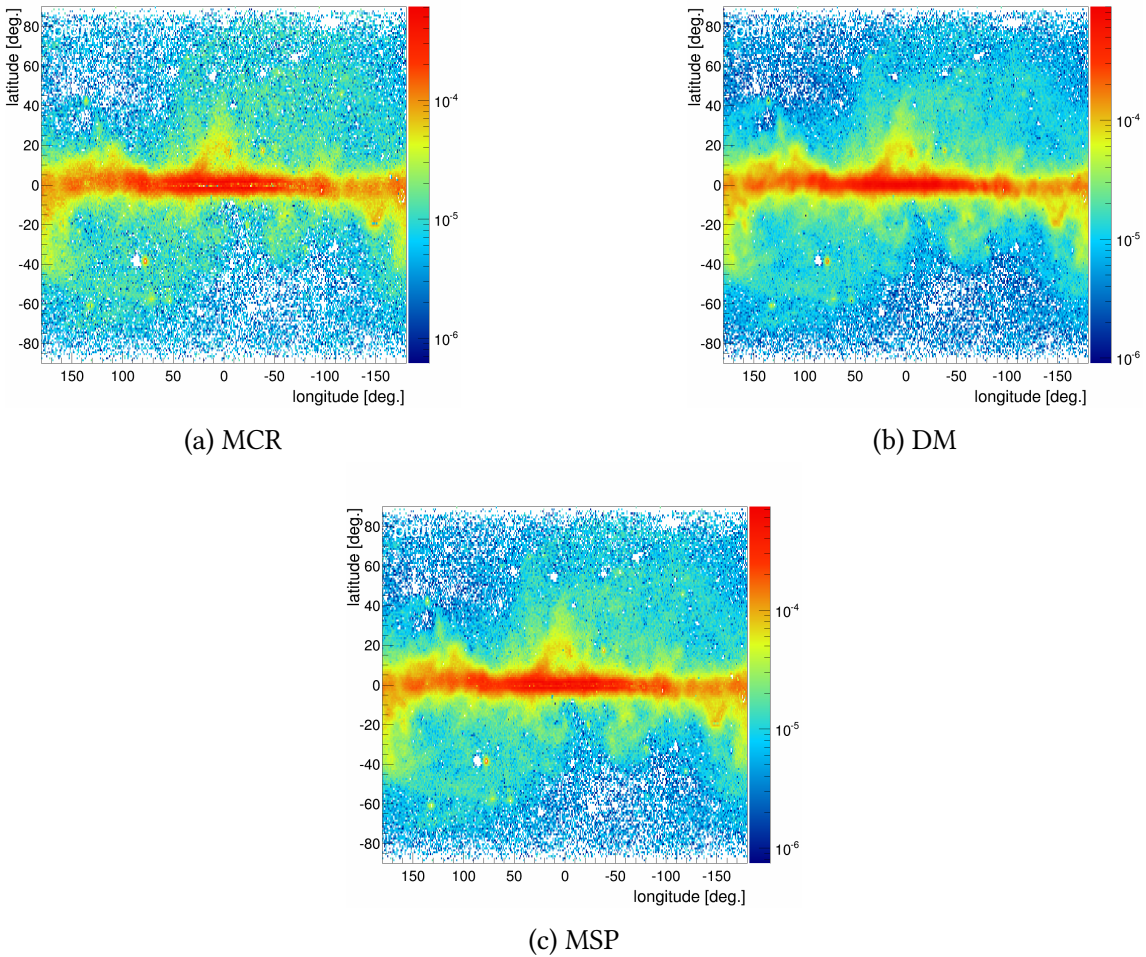


Figure 4.1.: PCR spatial distribution with a MCR (a), a DM (b) and a MSP (c) fit. The galaxy disk and matter distribution is clearly visible. With MCR and to a lesser extend MSP, a drop in flux can be observed in the disk, below two degrees in latitude. This could be the excess component tracing MCs that take other PCR, tracing the propagated CRs.

### 4.1.2. IC flux distribution

The inverse compton scattering component is directly proportional to the ISRF and the electrons CR. Electrons are present everywhere in the galaxy, and the ISRF is dominant in the GC for the UV range, but follows the dust in the IR range and is isotropic in the radio. This distribution should be visible in the IC component of the fit. Indeed, a spherical distribution can clearly be identified for the three different fits with DM, MCR and MSP (Fig. 4.2). Nonetheless, there is a noticeable difference in the disk between the IC distribution for the MCR and DM fits and the MSP fit. In the MCR and DM fit, the disk presents a high IC flux when the MSP fit does not. On the contrary, the MSP fit presents a clear dip in the galactic disk. This gap is unexpected, since the ISRF is supposed to be the strongest in the disk, and the diffuse electrons are also produced mainly here. This effect could come from the shape of the MSP spectrum at low energies. Indeed, being softer than MCR and DM, and having a higher contribution in the disk where the excess is present, the fit overshoot the low energies under 1 GeV. This does not leave any space for an IC component that is also very soft. This is shown in figure B.4 where the only fit that does not need IC in the CMZ is the MSP fit.

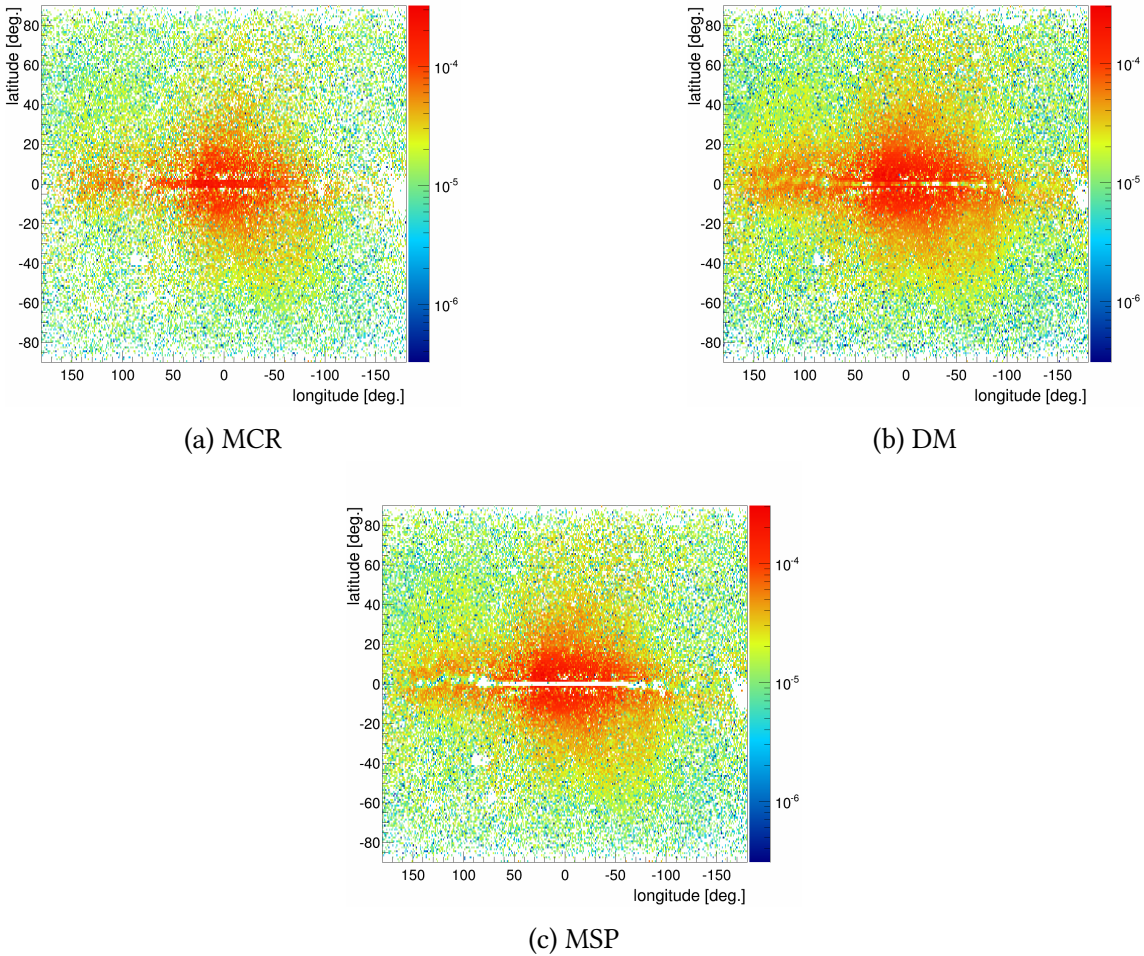


Figure 4.2.: IC spatial distribution with a MCR (a), a DM (b) and a MSP (c) fit.

### 4.1.3. BR flux distribution

The BR component is linked to the CR electron density along the line of sight and the gas distribution in the galaxy. It should then be present everywhere. It is what can be observed in Fig. 4.3, but some features are remarkable. Mainly the decrease of the flux in the disk. This gap in the disk is not fully understood, but a fine tuning of the CR electron spectrum might solve the issue. Depending on the fit, the average flux over the whole sky is also changing. The BR component is a lot more present with the MCR fit than with DM, which in turn presents more BR than the MSP fit. The fact that the MSP fit does not use a lot of BR is consistent with the fact that the MSP spectrum is very soft at low energies. Since BR is also dominant at these energies, both cannot have a high flux at the same time. The fit must do concession in order to use them both, like for the IC component.

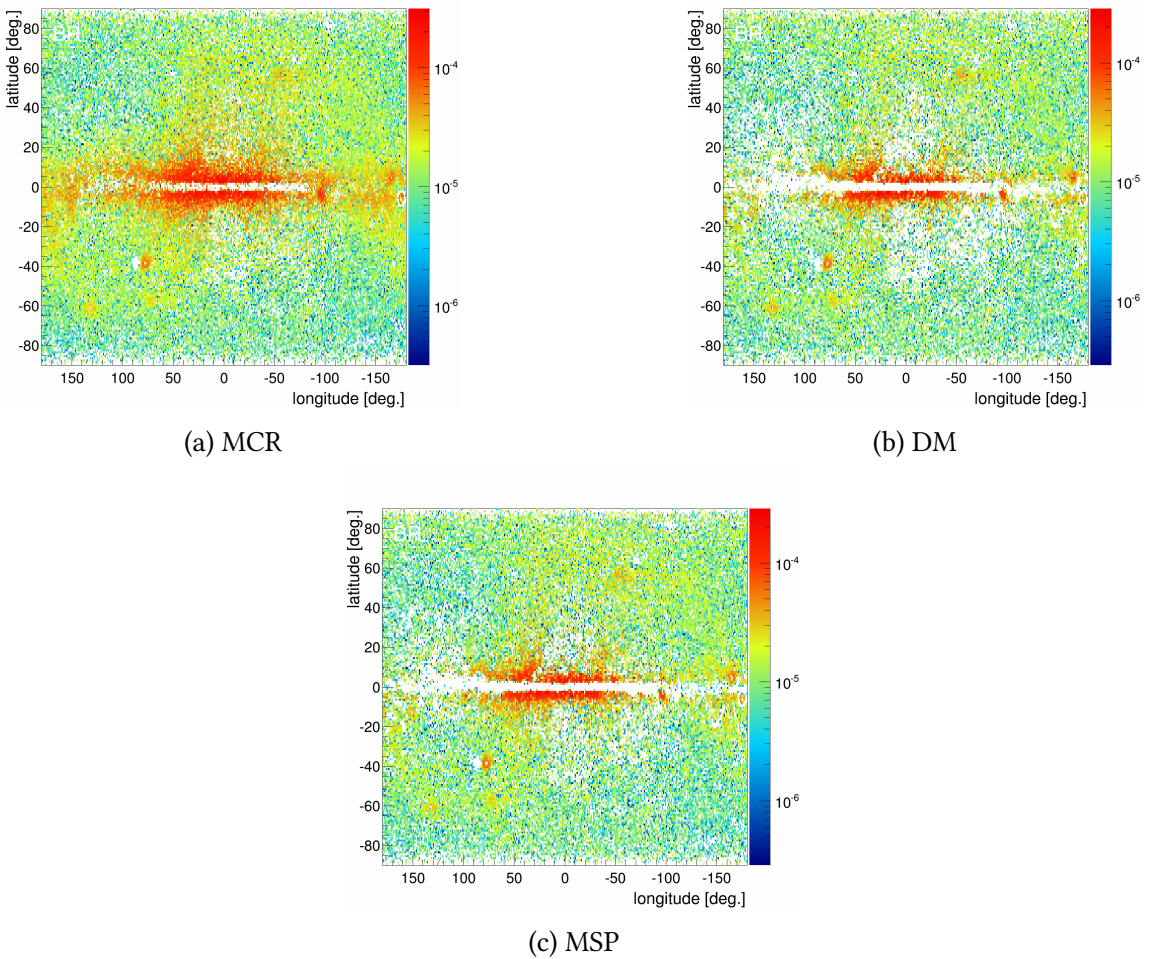


Figure 4.3.: BR spatial distribution with a MCR (a), a DM (b) and a MSP (c) fit.

#### 4.1.4. SCR flux distribution

The SCR distribution is expected to follow the disc, where point sources can still remain, and the bubbles, where the proton CR spectra is harder. And indeed, the spatial distribution obtained in the three different fits are similar and correspond perfectly to the expectations (Fig. 4.4). A lot of cones with SCR outside of these regions still remain, but this can be considered as noise, the binning being small and the statistical uncertainties relatively big. This effect disappears completely when using a larger binning., and only the bubbles and the disk remains visible with SCR.

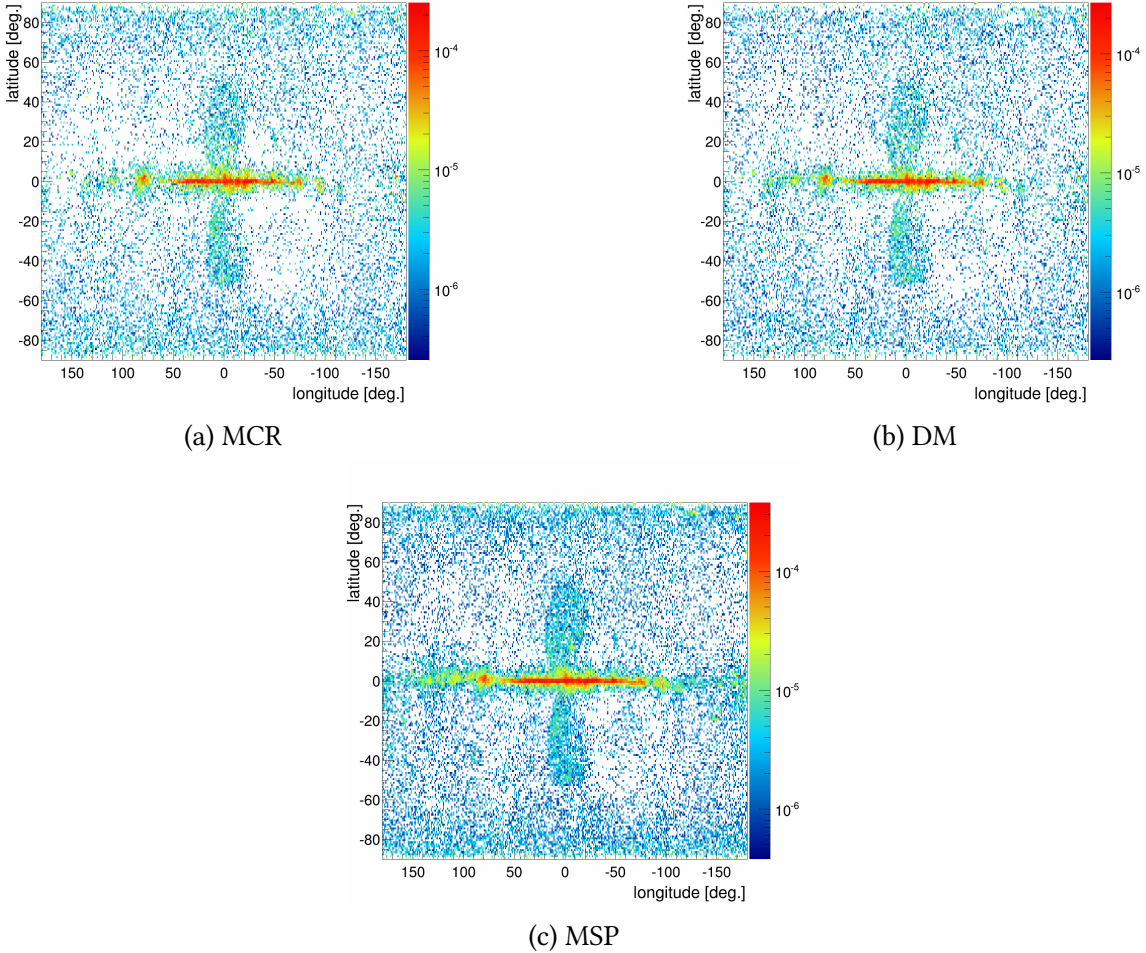


Figure 4.4.: SCR spatial distribution with a MCR (a), a DM (b) and a MSP (c) fit.

## 4.2. Correlation between SCR, MCR and point sources

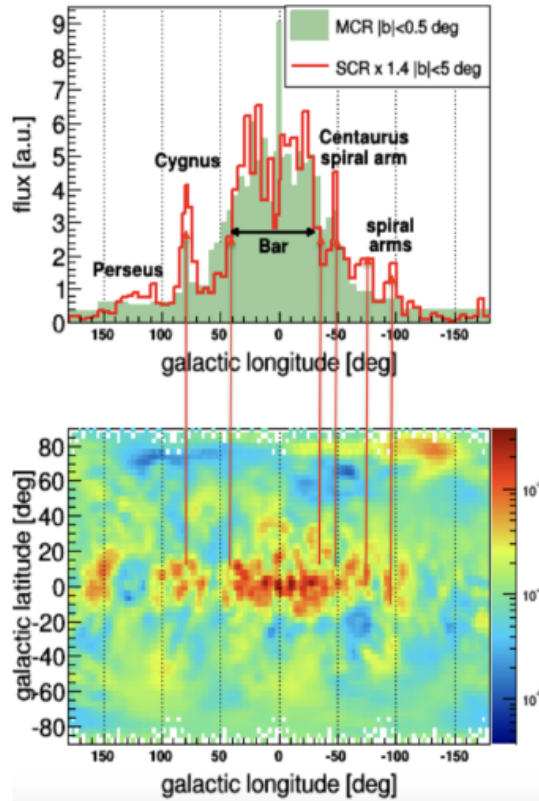


Figure 4.5.: The longitude distribution of the fluxes from the SCR and MCR templates, which have a similar morphology, as expected since both are connected to MCs. The lower panel shows the  $^{26}\text{Al}$  sky map [18] [19], which is correlated with the top panel, as indicated by the vertical arrows. This correlation is expected, since both, the  $^{26}\text{Al}$  flux and the SCR flux, are tracers of cosmic ray sources. Image taken from [1].

Since sources are expected to reside inside MCs one expects a strong correlation in the spatial distributions of the SCR fluxes and the MCR fluxes, i.e. if there is a long tail in the gamma-ray spectra above 30 GeV, one expects a simultaneous shift in the maximum of the spectrum from 0.7 up to 2 GeV. The strong correlation between the SCR and MCR fluxes is indeed observed, as shown in the top panel of Fig. 4.5. Here the gamma-ray fluxes from the SCR (MCR) templates are integrated over a latitude range of  $|b| < 5^\circ(0.5^\circ)$ , respectively. The larger latitude range for the SCR component is just to increase the statistics of the SCR fluxes, since the sources can have outflows towards higher latitudes, as suggested by the broad latitude distribution of  $^{26}\text{Al}$  in the bottom panel of Fig. 4.5. The strong correlation between the SCR fluxes, MCR fluxes and  $^{26}\text{Al}$  fluxes is emphasized by the vertical arrows in Fig. 4.5 between the sky map of the  $^{26}\text{Al}$  line (bottom panel) and the longitude distribution of the SCR and MCR fluxes (top panel). This correlation is observed when using a DM or a MSP component instead of MCR. But, as for the correlation with the CO emission, it is only expected in the case of MCR.

### 4.3. Adding an break in electron CR spectrum

The theory behind the MCR component involves a magnetic cut-off for low rigidity CR protons that changes the gamma-ray spectrum at low energies. Such a cut-off only depends on the rigidity of the CR and the intensity of the electromagnetic field. So there is no reason for it to be only applied to protons, and not to electrons. This is the reasoning that led to the introduction of a new template, called MBR in the fit, equivalent to the BR template, but calculated from a different electron CR spectrum. The reason it was not used before is the low percentage of electron CRs compared to protons. This MBR component should be less present than MCR. This new CR spectrum is composed of two different power laws for high and low energies, joining at the break position. It has the exact same spectral indexes than the electron CR spectrum used for IC and BR (0.81 below the break and 3.21 above), but the break is moved up, between 6 and 14 GeV, to stay consistent with the MCR break. The fit method is the same, and the MBR break is fixed to the MCR brake in a given region. This way, the magnetic cut-off is applied the same way to the electrons and protons CR in the same region. Once again, this component is expected to follow the MCs distribution, as expected with MCR.

A MIC component was tested as well, but it was not kept in the fit. This component would have been an IC component with a break between 6 and 14 GeV in the electron spectrum, following the same reasoning than for MBR. The reason it was not kept is that it did not improve the fit at all. It is very close from the initial IC component, almost indistinguishable by the fit, and do not bring anything new.

Figure 4.6 shows the results of a fit using all background components, SCR, MCR and MBR, and its effect on the BR component. As with the MCR fit 3.7a, the CMZ is very well fitted by the model. There is still no BR contribution, but the MBR template is present. The spatial distribution of BR is also very similar to the MCR fit (see Fig. 4.3a), with a lower flux in the disk. On the contrary, the MBR component is mainly present in the disk and the GC, as expected, where MCs are supposed to change the electron CR spectrum. The bubbles also appear to show a MBR contribution that is not predicted by the theory behind MBR. This can be interpreted as a hint that the model is not perfect, and that the different templates do not only play their theoretical role, but can also be used where they are not supposed to. In that case, a fine tuning of the CR spectra used to get the gamma-rays templates is required to get the theoretical distributions.

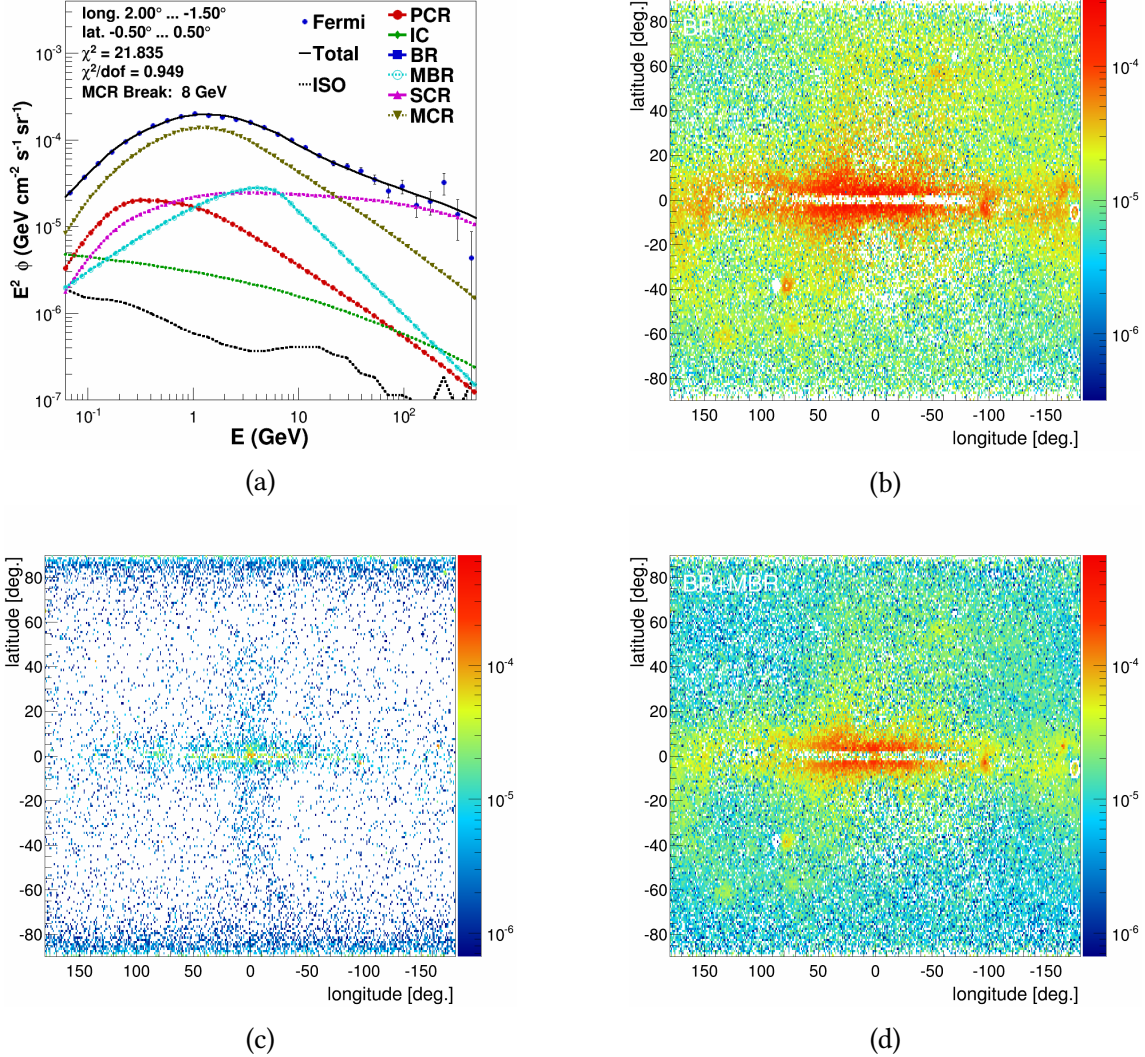


Figure 4.6.: Results of the fit using a MBR component. (a) CMZ spectrum. The MBR component has a major contribution around 5 GeV. Compared to Fig. B.4b, the fit slightly improves with a smaller  $\chi^2$  value. (b) BR flux distribution. It resembles closely the distribution before adding MCR, with a strong gap in the disk (see Fig. 4.3a). (c) MBR flux distribution. It is strong in the GC and the disk, but decreases rapidly around. The pole structures are artifacts due to a lack of statistics at high latitudes. (d) Sum of BR (b) and MBR (c) flux. The MBR contribution is not strong enough to fill the BR gap in the disk.

## 4.4. Mixing MCR and DM

MCR is a good solution to the gamma-ray GeV excess in the GC, and could replace the first hypotheses of a DM halo or hidden MSPs. Yet, the DM theory is strongly supported by other measurements, for example the rotation curves of galaxies [11] [12], and is one of the most important question of modern physics. And the fact that it is not the primary cause of the effect observed here does not mean it does not exist. And under the hypothesis that MCR is really the cause of the excess, the fit could put strong limits on the DM models. This section will present a few ways to study the current DM WIMP model using the fit method of this thesis.

### 4.4.1. DM and MCR in the same fit

A first idea is to give the fit a DM and a MCR template with free scaling factors and let it combine them to find the best  $\chi^2$  value. Taking a 52.3 GeV WIMP mass and the MCR template with free breaks between 6 and 14 GeV, the fit has the choice between the two. The results are in favor of MCR (Fig 4.7), almost ignoring the DM component. Only the DM distribution is shown here, because all the other looks exactly like the MCR fit. This could be predicted from the previous comparisons of the  $\chi^2$  distribution for a MCR or a DM fit that showed a clear preference toward MCR, at least in the disk. Indeed, the  $\chi^2$  map of a MCR fit is flat around one, even in the disk, whereas a DM fit does not work well for small latitudes. Here the contribution of DM is very small and plays a minor role in the fit, it is therefore hard to conclude anything from it. A minor change in a template or more statistics in the future might totally change the DM contribution obtained here.

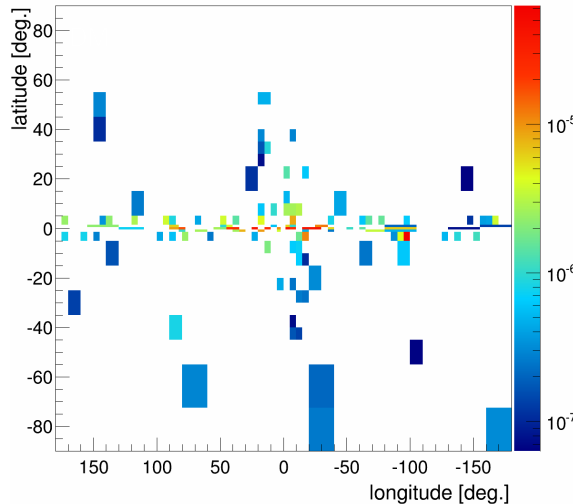


Figure 4.7.: DM flux distribution fitting all background components, SCR, MCR and DM.

DM is almost not used anywhere, thus using DM or not does not change the results of the fit. The adapted binning of 797 cones is used here because the statistics are too low in a one by one degree binning to show the DM contribution.

#### 4.4.2. Adding DM afterwards

The second idea that comes to mind is to take the MCR template for granted, and see if there is space to add a DM contribution after fitting with MCR. In other words, a first fit is performed with the classical templates (PCR, IC, BR), the source (SCR) and the MCR templates. Once the best  $\chi^2$  is found, the fit tries to add a DM template to improve the model. Following the Ockham's razor principle, the least amount of contributions are accepted as true, and any additional component must be treated carefully. This way, the necessity of a DM template is checked, and its contribution can not be mistaken for a classical one.

The results are clear, the fit adds only very few DM to the model (Fig. 4.8). As in the previous section, this could be expected since the  $\chi^2$  of the MCR only fit is already good. Only very small changes could improve it without changing the classical contributions. DM is used sparsely all over the disk, but no spherical shape can be distinguished. Again, it is hard to conclude anything before having better data quality or a better model.

Anyway, further studies of this kind could help to determine properties of DM particles, like their mass.

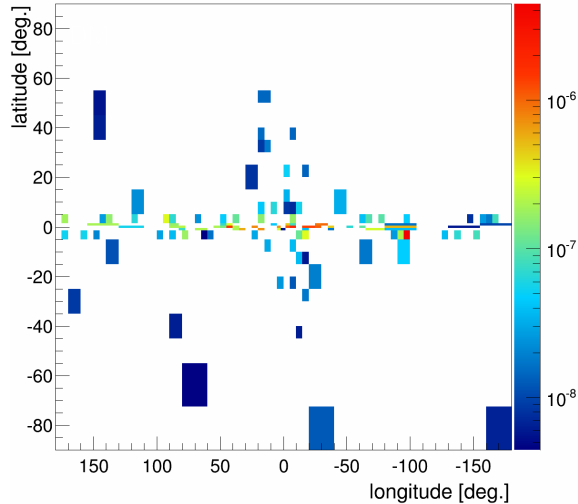


Figure 4.8.: DM flux distribution when adding the DM component after fitting MCR. The initial MCR fit being already very good with a low  $\chi^2$ , DM cannot bring too much to the model. The adapted binning of 797 cones is used here because the statistics are too low in a one by one degree binning to show the DM contribution.

## 5. Conclusion

Using a simple, well constrained, fitting method, the entire gamma-sky was modeled in a wide energy range. This allowed a spatial as well as a spectral study to be developed around the GC gamma-ray excess. High spatial resolution up to one by one degree bins were achieved, allowing a very detailed study of the excess distribution.

Starting from the adopted model composed of three components, PCR, BR and IC, improvements were made to solve its two main issues. First, the addition of a source template (SCR) improved the fit at high energies in the disk and the bubbles (see section 3.2 or figure 3.5). Indeed, a harder spectrum was needed above 10 GeV, and a harder CR proton spectrum worked perfectly. The flux distribution from this new component follows exactly its expected distribution.

Then, three hypothesis for the GC gamma-ray excess were tested and compared, namely the dark matter (DM), milli-second pulsars (MSP) and molecular clouds cut-offs (MCR). The results makes the MCR hypothesis stand out from DM and MSP. First, the spectral shape of the MCR component is more adapted to the excess spectral shape, thus allowing high energies as well as low energies to be fitted properly for any given region of the sky. On the contrary, MSP and DM have spectral features that do not allow a proper fit everywhere, especially the very soft spectrum above 10 GeV, making them insignificant for higher energies. Second, comes the general spatial distribution of the excess component in the fits. All three looks alike, following the MCs distribution in the galaxy when only MCR is supposed to do so. Indeed, DM and MSP are expected to be distributed spherically around the GC, and they have no reasons to follow the galactic matter distribution. And finally, when looking at the details of the GC, and in particular the CO distribution, one can see a correlation between the excess component flux and the CO emission (see section 3.5 and figure 3.10). This last result gives again a clear indication in favor of MCR, since it is the only component directly linked with molecular clouds. Overall, MCR was preferred by the fit and gives a explanation for the GC excess while staying in the standard model of physics.

Several path were followed to try and improve the model where MCR is the excess component. A new component (MBR) was introduce, following the same reasoning than MCR, but with the electron CR. Since electron proportion is smaller, the effect of this new template is expected to be smaller. The quality of the fit does not change significantly

since it was already good allowing only for relatively small changes. Accepting the MCR hypothesis, one can also look for DM using this fitting method. This scenario was tested but did not give significant results, as MCR is always a better choice for the fit. DM is almost not contributing to the gamma-ray flux in the galaxy, and no spherical distribution could be observed. This does not disprove the existence of DM as WIMPs, but could help to study it. In latter work, an upper limit could be found on the WIMPs density and cross section for example. The model developed in this work can still be improved, and strange structure in some component spatial distribution need further discussion.

The main result to take away from this work is that molecular clouds could explain the presence of the Fermi GeV excess around the GC and give a good model for the diffuse gamma-ray emission for the entire galaxy.

# Acknowledgments

I would like to thanks all the people who worked with me during my master degree. Special thanks go to my german tutors Pr. Wim de Boer and Pr. Iris Gebauer for their precious help and support. Of course Fabian, Alexander, Toni, Stefan and Niklas, who stood along my side in this year long battle against ROOT merit all my gratitude as well.

I would also like to thanks the UFA-DFH, who gave me the opportunity to do all this and learn (a little) German, along with all the professors from the UGA who taught me what I love.

Last but not least, I want to thank my family, Claire and every friend I met this year, around a slack or a beer, in Germany or France, for the good times we shared and your smiles that kept me going.



# Bibliography

- [1] de Boer, W.; Bosse, L.; Gebauer, I.; Neumann, A.; Biermann, P. L. *prd* **2017**, *96*, 043012.
- [2] Kevin Jardine, <http://galaxymap.org/drupal/node/171>, Version Date: 2018-04-10.
- [3] Rob Garner, [https://www.nasa.gov/mission\\_pages/GLAST/news/new-structure.html](https://www.nasa.gov/mission_pages/GLAST/news/new-structure.html), Version Date: 2018-10-04.
- [4] Hubble, E. *Contributions from the Mount Wilson Observatory / Carnegie Institution of Washington* **1926**, *324*, 1–49.
- [5] Kafle, P. R.; Sharma, S.; Lewis, G. F.; Bland-Hawthorn, J. *apj* **2014**, *794*, 59.
- [6] Su, M.; Slatyer, T. R.; Finkbeiner, D. P. *apj* **2010**, *724*, 1044–1082.
- [7] Ackermann, M. et al. *apj* **2014**, *793*, 64.
- [8] Planck Collaboration, et al. *A&A* **2014**, *571*, A13.
- [9] Liu, T.; Wu, Y.; Zhang, H. *apjl* **2013**, *775*, L2.
- [10] Bohlin, R. C.; Savage, B. D.; Drake, J. F. *apj* **1978**, *224*, 132–142.
- [11] Matthew Newby, <http://milkyway.cs.rpi.edu/milkyway/science.php>, Version Date: 2018-03-27.
- [12] Ford, W. K., Jr.; Rubin, V. C.; Roberts, M. S. *aj* **1971**, *76*, 22–24.
- [13] McKeough, J.; Hira, A.; Valdez, A. Theoretical Comparison Between Candidates for Dark Matter. APS April Meeting Abstracts. 2017; p C2.004.
- [14] Navarro, J. F.; Frenk, C. S.; White, S. D. M. *The Astrophysical Journal* **1997**, *490*, 493.
- [15] Jungman, G.; Kamionkowski, M.; Griest, K. *Physics Reports* **1996**, *267*, 195 – 373.
- [16] Wu, C. S. *jgr* **1984**, *89*, 8857–8862.
- [17] Prantzos, N.; Diehl, R. *physrep* **1996**, *267*, 1–69.
- [18] Bouchet, L.; Jourdain, E.; Roques, J.-P. *The Astrophysical Journal* **2015**, *801*, 142.
- [19] Integral-SPI, The data were downloaded from: <http://sigma-2.cesr.fr/integral/aluminium-map&source>, Version Date: 2015.
- [20] Giacinti, G.; Kachelrieß, M.; Semikoz, D. V. *prd* **2015**, *91*, 083009.

- [21] Gebauer, I. An anisotropic model for galactic cosmic ray transport and its implications for indirect dark matter searches. Ph.D. thesis, Karlsruher Institut für Technologie (KIT), 2010.
- [22] Daniel, R. R.; Stephens, S. A. *ssr* **1975**, *17*, 45–158.
- [23] Jansson, R.; Farrar, G. R. *The Astrophysical Journal* **2012**, *757*, 14.
- [24] Gleeson, L. J.; Axford, W. I. *apj* **1968**, *154*, 1011.
- [25] Arlt, R.; Rüdiger, G. *mnras* **2011**, *412*, 107–119.
- [26] Inceoglu, F.; Simoniello, R.; Knudsen, M. F.; Karoff, C. *aap* **2017**, *601*, A51.
- [27] Crutcher, R. M. *Annual Review of Astronomy and Astrophysics* **2012**, *50*, 29–63.
- [28] Berezinsky, V.; Gazizov, A. Z. *The Astrophysical Journal* **2006**, *643*, 8.
- [29] Williams, J. P.; Blitz, L.; McKee, C. F. *Protostars and Planets IV* **2000**, 97.
- [30] Störmer, C. *zap* **1930**, *1*, 237.
- [31] Ivlev, A. V.; Dogiel, V. A.; Chernyshov, D. O.; Caselli, P.; Ko, C.-M.; Cheng, K. S. *apj* **2018**, *855*, 23.
- [32] W. Hanlon, <http://www.physics.utah.edu/~whanlon/spectrum.html>, Version Date: 2018-04-10.
- [33] Hillas, A. M. *Annual Review of Astronomy and Astrophysics* **1984**, *22*, 425–444.
- [34] Biermann, P. L. *Nuclear Physics B - Proceedings Supplements* **1995**, *43*, 221 – 228.
- [35] Humboldt State University, [http://gsp.humboldt.edu/o1m\\_2015/Courses/GSP\\_216\\_Online/lesson2-1/atmosphere.html](http://gsp.humboldt.edu/o1m_2015/Courses/GSP_216_Online/lesson2-1/atmosphere.html), Version Date: 2018-03-27.
- [36] Atwood, W. B. et al. *The Astrophysical Journal* **2009**, *697*, 1071.
- [37] Kanbach, G. et al. *ssr* **1989**, *49*, 69–84.
- [38] Calore, F.; Cholis, I.; Weniger, C. *Journal of Cosmology and Astroparticle Physics* **2015**, *2015*, 038.
- [39] Fermi-LAT Collaboration, *ArXiv e-prints* **2017**,
- [40] Yang, R.; Aharonian, F.; Evoli, C. *prd* **2016**, *93*, 123007.
- [41] Fermi Science Tools Software Version v10r0p5, <https://fermi.gsfc.nasa.gov/ssc/data/analysis/software/v10r0p5.html>, Version Date: 2017-09-09.
- [42] Acero, F. et al. *apjs* **2015**, *218*, 23.
- [43] Evoli, C.; Gaggero, D.; Grasso, D.; Maccione, L. *Journal of Cosmology and Astroparticle Physics* **2008**, *2008*, 018.
- [44] Aguilar, M. et al. *Phys. Rev. Lett.* **2015**, *114*, 171103.
- [45] Gleeson, L. J.; Axford, W. I. *apj* **1968**, *154*, 1011.
- [46] Biermann, P. L.; Becker, J. K.; Dreyer, J.; Meli, A.; Seo, E.-S.; Stanev, T. *The Astrophysical Journal* **2010**, *725*, 184.

- [47] Hillas, A. M. *Journal of Physics G: Nuclear and Particle Physics* **2005**, *31*, R95.
- [48] Gondolo, P.; Edsjo, J.; Ullio, P.; Bergstrom, L.; Schelke, M.; Baltz, E. A. *Journal of Cosmology and Astroparticle Physics* **2004**, *2004*, 008.
- [49] Gondolo, P.; Edsj  , J.; Ullio, P.; Bergstrom, L.; Schelke, M.; Baltz, E. A. *New Astronomy Reviews* **2005**, *49*, 149 – 151, Sources and Detection of Dark Matter and Dark Energy in the Universe.
- [50] Daylan, T.; Finkbeiner, D. P.; Hooper, D.; Linden, T.; Portillo, S. K.; Rodd, N. L.; Slatyer, T. R. *Physics of the Dark Universe* **2016**, *12*, 1 – 23.
- [51] Hooper, D.; Linden, T. *prd* **2011**, *84*, 123005.
- [52] Boer, W. D. *Surveys in High Energy Physics* **2006**, *20*, 19–45.



# List of Figures

1.1.	The milky Way from different angles. . . . .	3
1.2.	Rotation curve of the Milky Way. . . . .	5
1.3.	Energy losses over time of CR particles. . . . .	8
1.4.	CR spectrum as observed on Earth. . . . .	10
2.1.	Gamma-ray sky by Fermi. . . . .	15
2.2.	Systematic errors for the Fermi LAT . . . . .	18
2.3.	Initial CR spectra. . . . .	19
2.4.	Variations of the IC and BR template over the sky. . . . .	20
2.5.	Comparison of gamma-ray templates . . . . .	21
2.6.	Isotropic calibration. . . . .	22
3.1.	Representation of the GC excess. . . . .	25
3.2.	CMZ fitted with the background components. . . . .	26
3.3.	Comparison of EGRET and Fermi results . . . . .	28
3.4.	Distribution of the SCR only fit. . . . .	29
3.5.	Spectra before and after adding SCR in a bubble. . . . .	30
3.6.	SCR fit spectra. . . . .	31
3.7.	MCR fit spectra. . . . .	32
3.8.	Spatial distribution of CO, MCR, DM and MSP. . . . .	33
3.9.	DM and MSP spectral indexes graph. . . . .	34
3.10.	CO and MCR correlation plots. . . . .	37
4.1.	PCR spatial distributions. . . . .	40
4.2.	IC spatial distributions. . . . .	41
4.3.	BR spatial distributions. . . . .	42
4.4.	SCR spatial distributions. . . . .	43
4.5.	Correlation between SCR, MCR and point sources . . . . .	44
4.6.	Results of the fit with MBR. . . . .	46
4.7.	DM distribution for a fit using DM and MCR . . . . .	47
4.8.	DM distribution after fitting a MCR excess . . . . .	48
A.1.	Isotropic template convergence. . . . .	64
B.2.	Background components flux distribution in the background only fit . .	65
B.3.	Components flux distribution in the background and source fit . . . . .	66
B.4.	$\chi^2$ distributions and CMZ spectra for the MCR, DM and MSP fits. . . . .	67
B.5.	Correlation of DM and MSP to CO emission. . . . .	68
C.6.	Skymap of the PCR and MCR sum. . . . .	69



# Appendix

## A. Method

Listing 5.1: Bash script details for the treatment of the Fermi LAT data.

```
#First, install the Fermi science tools from: https://fermi
.gsf.c.nas.a.gov/ssc/data/analysis/software/
#All I'm saying here is better explained in analysis thread
: https://fermi.gsfc.nasa.gov/ssc/data/analysis/scitools
/ You can look at the following threads: Extract LAT
Data, Using LAT All-sky Weekly Files, (Un)Binned
Likelihood Tutorial
#Also every command has a documentation at this address:
https://fermi.gsfc.nasa.gov/ssc/data/analysis/scitools/
help/<name of the command>.txt
fileBase="Base_name_of_all_files_produced_in_this_run"
spacecraft="
    location_of_the_spacecraft_file_containing_positions_and_infos_about_
"
#Some numbers that are used multiple times:
number_of_pixels_in_lon=720
number_of_pixels_in_lat=360
pixel_size=0.5

#Select the events from the weekly files listed in
file_list.txt. (ra, dec) is the galactic center
coordinates in ICRS system, a radius of 180 to select
the whole sky, and the energy bounds. The one here
correspond to the energy bound of the Fermi diffuse
model. You might run into troubles later if you try to
use it with energies out of this range
gtselect evclass = 256
    evtype = 3 \
    infile = file_list.txt \
```

```

outfile = $fileBase.fits \
ra = 266.4049882865447 \
dec = -28.93617776179147 \
rad = 180 \
tmin = INDEF \
tmax = INDEF \
emin = 58.4731 \
emax = 513056 \
zmax = 90
#Disregard all events registered out of the Good Time
#Intervals of the spacecraft, with the cut recommended by
#Fermi peoples
gtmktime scfile = $spacecraft \
filter = "DATA_QUAL>0 && LAT_CONFIG==1 && ABS(
    ROCK_ANGLE)<52" \
roiCut = no \
evfile = $fileBase".fits" \
outfile = $fileBase"_gtmktime.fits"
#Making the first map from the events. All options are on
#the web. The settings of this map are reused later for
#the exposure for example.
gtbin algorithm = "CCUBE" \
evfile = $fileBase"_gtmktime.fits" \
outfile = $fileBase"_ccube.fits" \
scfile = $spacecraft \
nxpix = $number_of_pixels_in_lon \
nypix = $number_of_pixels_in_lat \
binsz = $pixel_size \
coordsys = GAL \
xref = 0. \
yref = 0. \
axisrot = 0 \
proj = "CAR" \
ebinalg = "LOG" \
emin = 59 \
emax = 513000 \
enumbins = 30
#Make a first exposure map with default settings. It can
#take a long time. Here the zmax=90 is to avoid the earth
#limbs contamination.
gtltcube zmax = 90 \
evfile = $fileBase"_gtmktime.fits" \
scfile = $spacecraft \
outfile = $fileBase"_ltcube.fits" \
dcostheta = 0.025 \
binsz = 1
#Bin the exposure map in the same binning than gtbin. The
#only difference is for the energy bins: It creates a map
#for every energy bin's "EDGE" when gtbin creates a map

```

---

```

for every energy bin's "CENTER". This can be changed via
  "bincalc" option but you need to let it on edge for
  later.

#You can also do once a full exposure map, even if you
analyze only a small sky region, if you don't change the
  cuts in gtselect you can then reuse it.

gtexpcube2 bincalc="EDGE" \
    infile = $fileBase"_ltcube.fits" \
    cmap = $fileBase"_ccube.fits" \
    outfile = $fileBase"_expcube.fits" \
    irfs = "CALDB" \
    nxpix = $number_of_pixels_in_lon \
    nypix = $number_of_pixels_in_lat \
    binsz = $pixel_size \
    xref = 0. \
    yref = 0. \
    axisrot = 0 \
    proj = "CAR" \
    coordsys = GAL \
    ebinalg = "LOG" \
    emin = 59 \
    emax = 513000 \
    enumbins = 30

#Now you can divide your gtbin map by your gtxpcube2 map
#to get a flux map! Use this:
ftpixcalc outfile = $fileBase"_flux.fits" \
    expr = a/b \
    a = $fileBase"_ccube.fits" \
    b = $fileBase"_expcube.fits"

#Now to subtract the point sources:
#Let allow energy dispersion now, it is better too soon
#than too late.

export USE_BL_EDISP=true

#Create an .xml file that lists all the point sources or
#diffuse sources you want to add to your model. Here I
#add all the point sources that could play a role in my
#maps (it knows it from the gtmktime file), but also the
#diffuse Fermi background (gll_iem_v06.fits) and the
#Fermi isotropic template (iso_P8R2_CLEAN_V6_v06.txt).
#You will have to comment them out by hand afterward in
#the $fileBase"_model.xml" file if you don't want them in
#your model. The point sources are taken from the 3FGL
#catalog (gll_psc_v16.fit), for a significance > 3.

python make3FGLxml.py gll_psc_v16.fit $fileBase"_gtmktime.
fits" \
    -o $fileBase"_model.xml" \
    -G $FERMI_DIR/refdata/fermi/galddiffuse/gll_iem_v06.fits
    \
    -g gll_iem_v06 \

```

```

-I $FERMI_DIR/refdata/fermi/galdiffuse/
    iso_P8R2_CLEAN_V6_v06.txt \
-i iso_P8R2_CLEAN_V6_v06 \
--extDir=$storage_path/processing/ \
-s 3.

#This will create a map of each source listed in your .xml
file with the same parameters than your gtbin map. You
have to do it at least once for the diffuse sources, but
point sources are done quickly and can be done later (
via option ptsrc = yes/no). This can take some time and
the output file is quickly very big with the point
sources.

gtsrcmaps scfile = $spacecraft \
    expcube = $fileBase"_ltcube.fits" \
    cmap = $fileBase"_ccube.fits" \
    srcmdl = $fileBase"_model.xml" \
    bexpmap = $fileBase"_expcube.fits" \
    outfile = $fileBase"_srccube.fits" \
    irfs = CALDB

#This OPTIONAL step is here to fit every point sources to
your data to try to improve the 3FGL catalog and
subtract a better model. You obviously need all
backgrounds from fermi, iso template point and diffuse
sources. This will create a new improved .xml file with
slightly different values for every point sources than
the one created by make3FGLxml.py. This take A LOT of
time for big regions and can not be done for the whole
sky at once. If you want to do it you need to cut the
sky in smaller regions and reassemble them again after.
That might not be worth it...

gtlike refit = no \
    plot = no \
    sfile = $fileBase"_gtlike.xml" \
    statistic = BINNED \
    cmap = $fileBase"_srccube.fits" \
    bexpmap = $fileBase"_expcube.fits" \
    expcube = $fileBase"_ltcube.fits" \
    srcmdl = $fileBase"_model.xml" \
    irfs = CALDB \
    optimizer = NEWMINUIT

#You can finally create a model map of the sources to
subtract. The point sources are calculated automatically
if they are not found in the gtsrcmaps file.

gtmodel srcmaps = $fileBase"_srccube.fits" \
    srcmdl = $fileBase"_model.xml" \
    outfile = $fileBase"_modelcube_ptsrc.fits" \
    irfs = CALDB \
    expcube = $fileBase"_ltcube.fits" \
    bexpmap = $fileBase"_expcube.fits" \

```

```
outtype = CCUBE
#You can finally subtract the gtmodel map from your gtbin
map via:
ftpixcalc outfile = $fileBase"_diffuse.fits" \
expr = a-b \
a = $fileBase"_ccube.fits" \
b = $fileBase"_modelcube_ptsrc.fits"
```

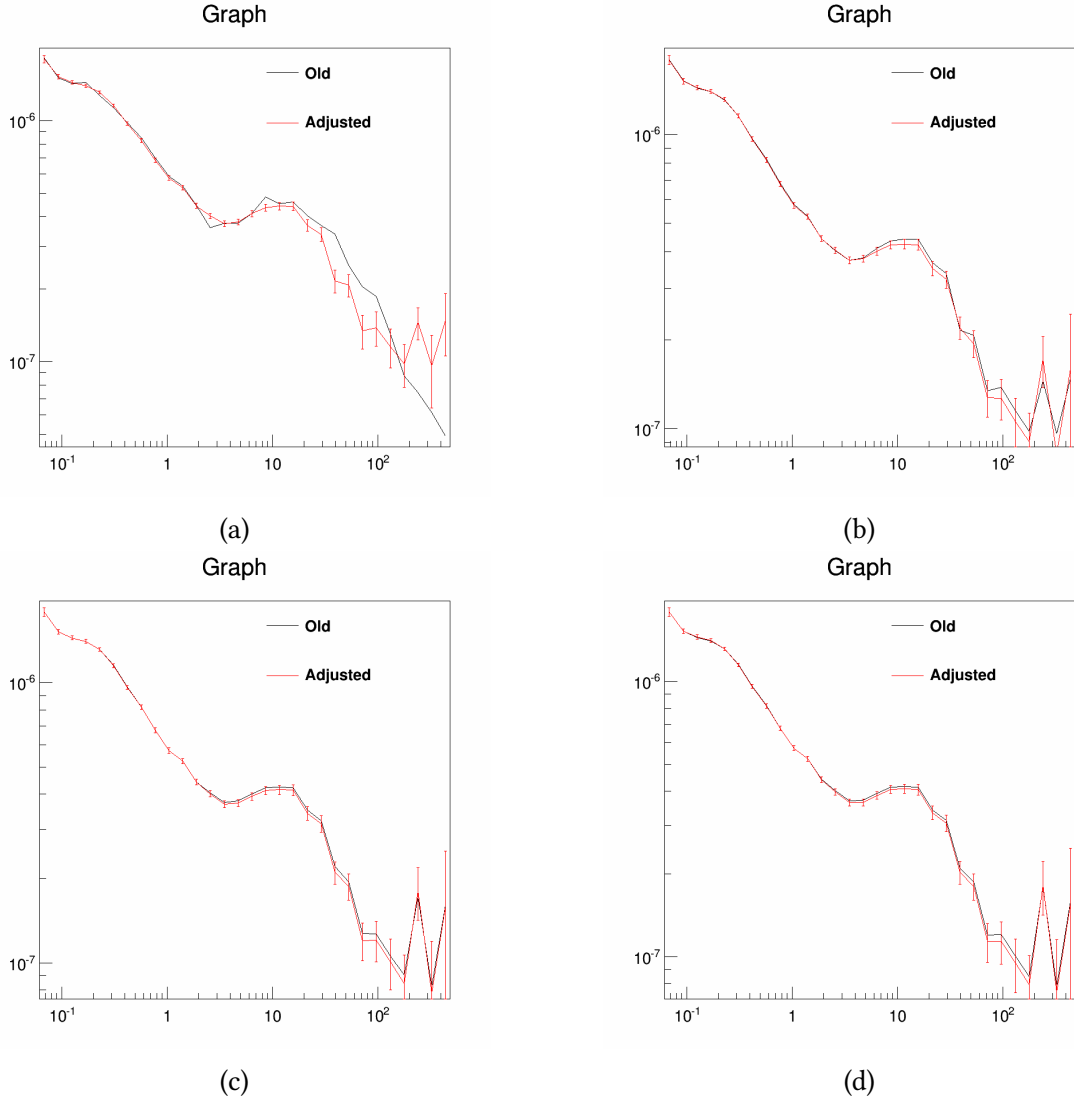


Figure A.1.: Isotropic recalibration process. Each graph compares the precedent (in black) and the new (in red) isotropic template. The initial template is the Fermi template iso\_P8R2\_CLEAN\_V6\_v06 that is given with the Fermi tools [41]. The convergence is reached after a few steps, even if high energies continue to fluctuate longer due to higher uncertainties.

## B. First results: Study of the excess

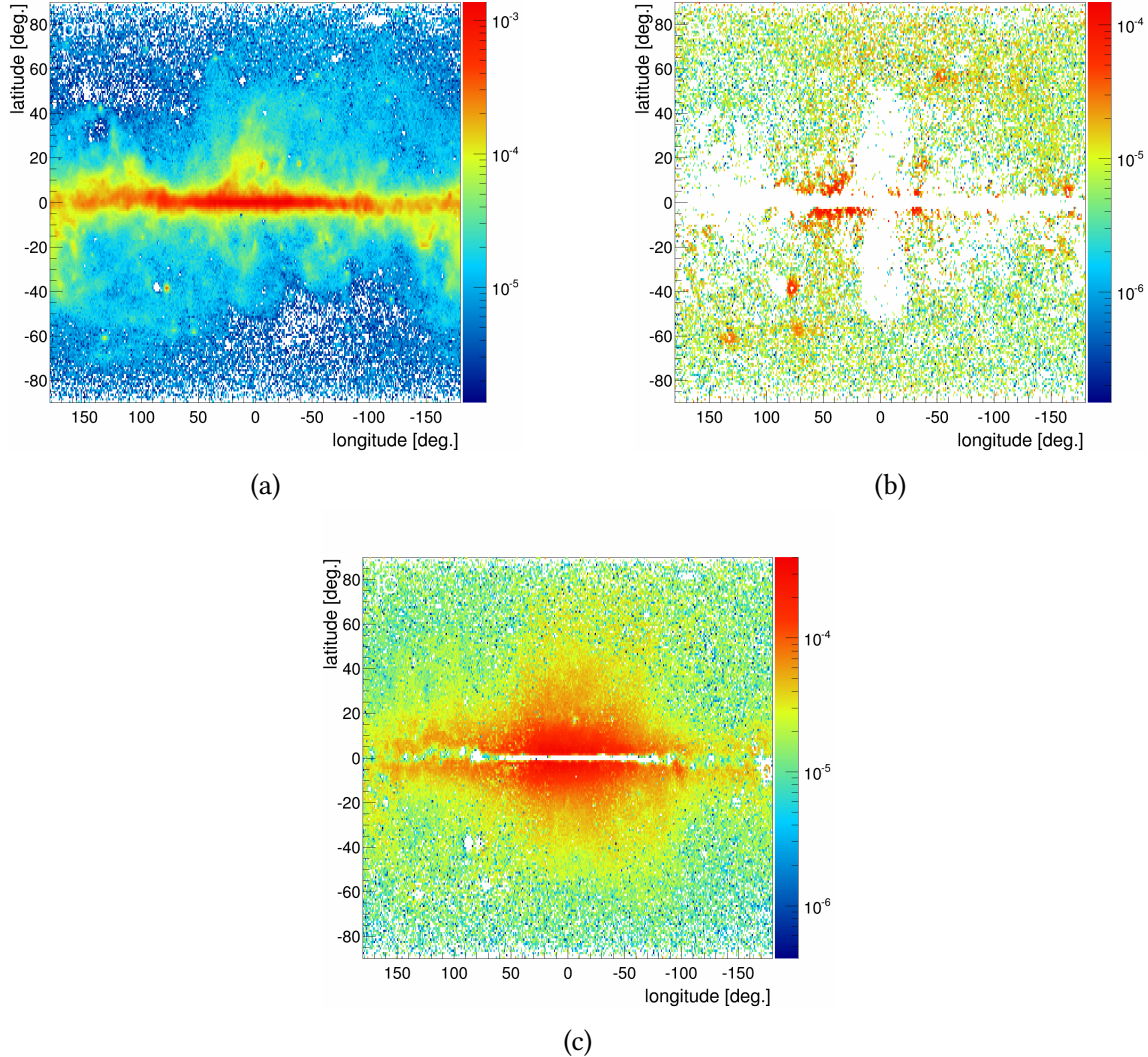


Figure B.2.: Background components flux distribution in the background only fit. (a) PCR distribution. (b) BR. (c) IC.

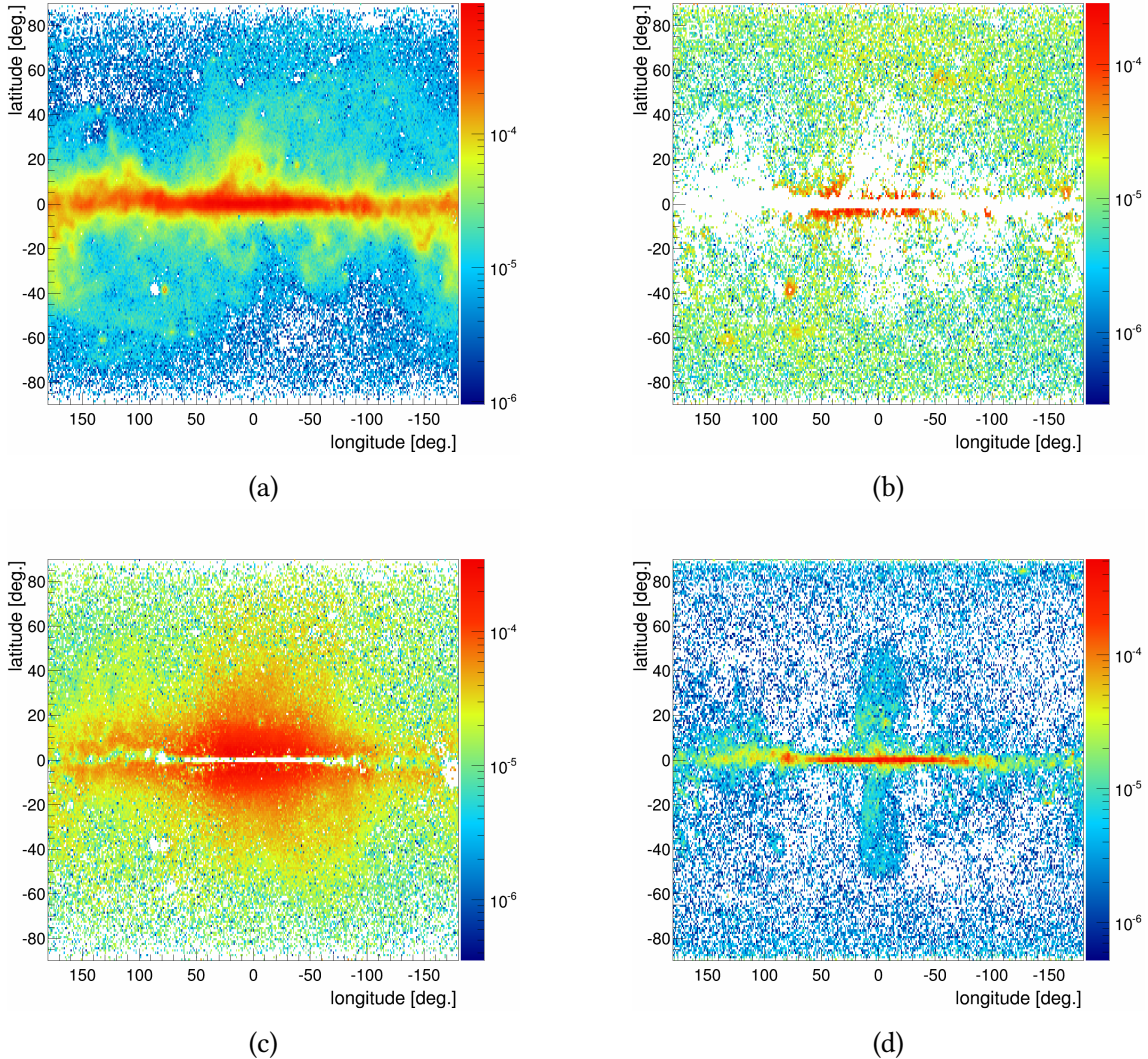


Figure B.3.: Components flux distribution in the background and source fit. (a) PCR distribution. (b) BR. (c) IC. (d) SCR.

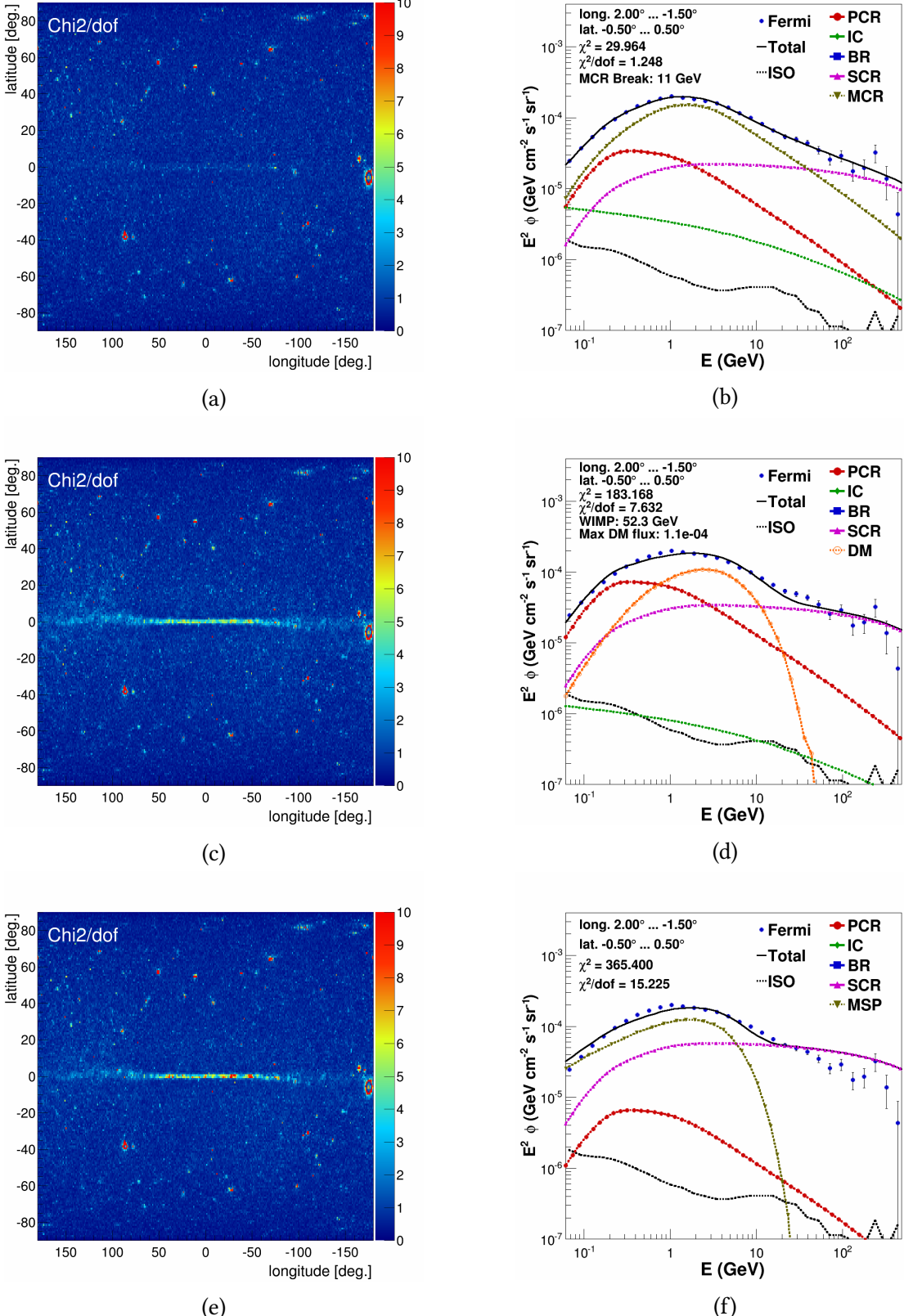
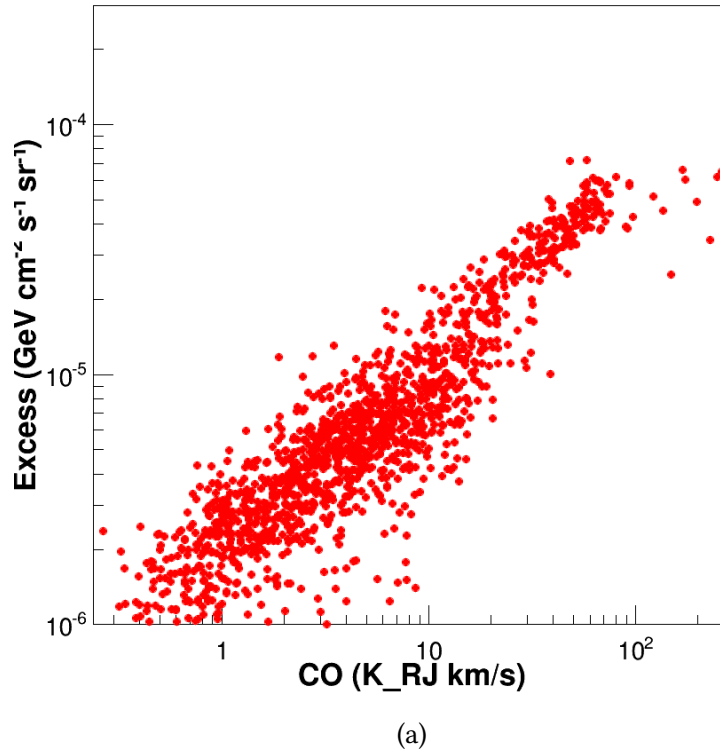
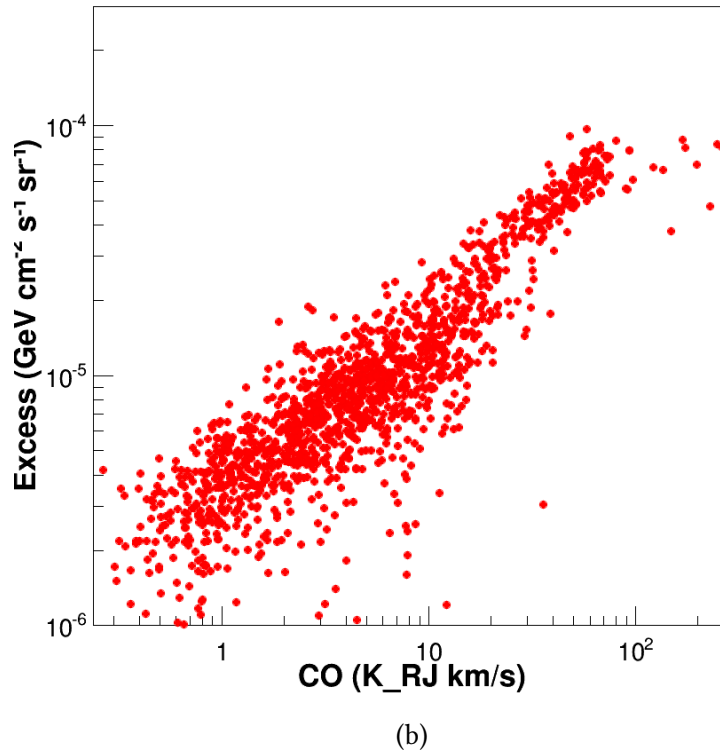


Figure B.4.: Comparison of the  $\chi^2$  distributions for the three excess fits (left column) and the CMZ region (right column). MCR (top row), shows a flat  $\chi^2$  distribution map, with almost no sign of the disk, and the CMZ is modelled at all energies. DM (middle row) does not fit the disk so well, and the CMZ is not described correctly above 10 GeV. MSP (bottom row) resemble a lot the DM model, with problems in the disk and a poor fit of the CMZ at high energies.



(a)



(b)

Figure B.5.: DM (a) and MSP (b) flux plotted against CO flux in every cones of one by one degree below two degrees in latitude. The correlation is clear and directly links the excess component to the galactic MCs.

## C. To go further: How to improve the model

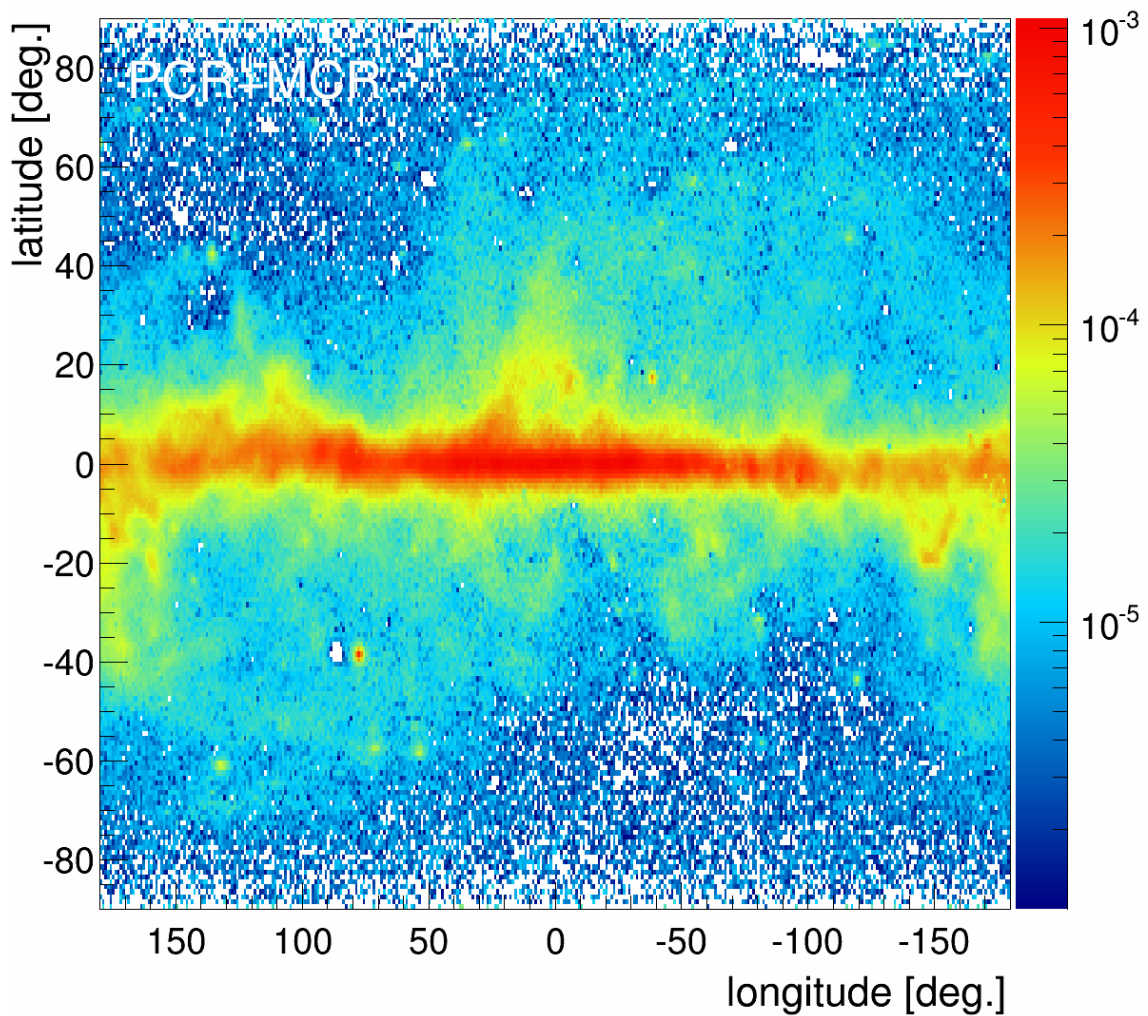


Figure C.6.: Sum of PCR and MCR spatial distribution for the MCR fit.

